








RESEARCH ARTICLE

10.1029/2024MS004525

The Efficient Integration of Dust and Numerical Weather Prediction for Renewable Energy Applications

Xi Chen¹ , Mei Chong^{1,2}, Shian-Jiann Lin³, Zhi Liang³, Paul Ginoux⁴ , Yuan Liang³ , Bihui Zhang⁵, Qian Song³, Shengkai Wang⁶, Jiawei Li¹ , and Yimin Liu^{1,2} 

¹National Key Laboratory of Earth System Numerical Modeling and Application, Institute of Atmospheric Physics, Chinese Academy of Sciences, Beijing, China, ²University of Chinese Academy of Sciences, Beijing, China, ³TianJi Weather Science and Technology Company, Beijing, China, ⁴Geophysical Fluid Dynamics Laboratory, NOAA/OAR, Princeton, NJ, USA, ⁵National Meteorological Centre, Beijing, China, ⁶Xiamen University, Xiamen, China

Key Points:

- The dust-dycore integrated iDust serves timely dust storm forecasts with high fidelity and long lead time for the renewable energy industry
- iDust captures extreme wind with high-resolution dynamics and accurately represents severe dust storms, even without initial dust data
- Accurate, high-resolution dynamics promise to enhance the skill of long-range dust transport simulations

Supporting Information:

Supporting Information may be found in the online version of this article.

Correspondence to:

X. Chen,
chenxi@lasg.iap.ac.cn

Citation:

Chen, X., Chong, M., Lin, S.-J., Liang, Z., Ginoux, P., Liang, Y., et al. (2025). The efficient integration of dust and numerical weather prediction for renewable energy applications. *Journal of Advances in Modeling Earth Systems*, 17, e2024MS004525. <https://doi.org/10.1029/2024MS004525>

Received 22 JUN 2024
Accepted 31 DEC 2024

Abstract The growing demand for renewable energy underscores the importance of accurate dust forecasting in regions with abundant wind and solar resources. However, leading real-time global numerical weather prediction (NWP) models often lack dust modules due to computational constraints. Current “Near-Real-Time” dust forecasting services can only run after the completion of NWP, failing to meet the timeliness requirements for reporting power generation plans to the grids. This work proposes a global dust-weather integrated (iDust) model development paradigm, efficiently incorporating dust modules into the dynamical core. Using about one-eighth additional computing power, iDust extends global 12.5 km resolution NWP with dust prediction capabilities. iDust’s forecasting abilities are evaluated against ECMWF CAMS forecast and NASA MERRA2 reanalysis, including verifications over China from March to May 2023 and three extreme dust events. Results show that iDust outperforms its counterparts in dust storm forecasting intensity and timing. Using iDust, global 12.5-km 10-day hourly dust storm forecast simulations initiated at 00UTC can produce results by 06UTC, enabling timely forecasting of severe dust storms with concentrations exceeding 1,000 $\mu\text{g}/\text{m}^3$. This novel capability of iDust can meet the urgent forecasting needs of the renewable energy industry for extreme dust conditions, supporting the green energy transition.

Plain Language Summary Leading economies need a green energy transition to avoid disastrous consequences caused by climate change. Barren regions are ideal for wind and solar power but are vulnerable to dust storms, which pose challenges for renewable energy operations. Traditional dust forecasting systems struggle with the added high computational cost of the sophisticated aerosol packages, leading to delayed, lower-resolution forecasts, and hindering the effective operation and risk management of renewable energy facilities. To address this problem, this work proposes iDust, an innovative paradigm that efficiently integrates dust storm forecasting into a global high-resolution weather forecasting model, utilizing only an additional one-eighth computational resources, extending the NWP with dust prediction capabilities. iDust enables timely forecasting of severe dust storms with concentrations exceeding 1,000 $\mu\text{g}/\text{m}^3$ and dust transport over long distances. The new paradigm of iDust integrated weather forecasting model construction expands the coverage of operational forecasting systems to include the prediction of damaging dust storms, providing in-depth customized support for emerging solar and wind power industries.

1. Introduction

The most significant impacts of dust on human activities are primarily felt in desert regions and urban areas. Dust interactions with short- and long-wave radiation alter atmospheric stability, circulation, and precipitation (Miller, Perlwitz, & Tegen, 2004; Miller & Tegen, 1999; Miller, Tegen, & Perlwitz, 2004; Miller et al., 2014). Besides its effects on climate, dust storms induce low visibility and hazardous air quality, impacting transportation, public health, and safety (Middleton, 2017; X. Zhang et al., 2016).

On the other hand, the leading economies worldwide are swiftly directing their focus toward transitioning to renewable energy, commonly called green energy, in a proactive effort to mitigate the disastrous consequences of climate change. Notably, vast barren regions between dust source regions and cities emerge as prime candidates for wind and solar energy industries, owing to their abundant year-round sunlight, superior wind resources, and ample land availability (Pourasl et al., 2023). Nevertheless, these environments do pose challenges for decision making due to their proneness to dust. Precise numerical weather forecasts that account for dust can significantly

© 2025 The Author(s). Journal of Advances in Modeling Earth Systems published by Wiley Periodicals LLC on behalf of American Geophysical Union. This is an open access article under the terms of the [Creative Commons Attribution-NonCommercial-NoDerivs License](https://creativecommons.org/licenses/by/4.0/), which permits use and distribution in any medium, provided the original work is properly cited, the use is non-commercial and no modifications or adaptations are made.

support renewable energy development. Such forecasts can minimize dust erosion on wind turbine blades, optimize cleaning plans for solar panels to conserve water in arid areas, and accurately forecast surface irradiance in weather environments affected by dust (Haywood et al., 2005; Maghami et al., 2016; Panat & Varanasi, 2022; Sarver et al., 2013; Schroedter-Homscheidt et al., 2013). Therefore, numerical weather forecasting should prioritize the renewable energy industry's need for timely, high-resolution dust forecasts.

However, major weather service centers conduct weather and dust forecast services separately. The United States National Oceanic and Atmospheric Administration (NOAA) recently upgraded its global forecasting system (GFS) using the FV3 model, achieving an average spatial resolution of 12.5 km globally (Harris et al., 2020). Its global aerosol forecast system, NGAC (Bhattacharjee et al., 2018; Lu et al., 2016; J. Wang et al., 2018), now GEFS-Aerosol (L. Zhang et al., 2022), is driven by the GFS with a lower resolution of 25 km. The European Centre for Medium-Range Weather Forecasts (ECMWF) uses the Integrated Forecasting System (IFS) to provide global weather forecast services, driven by traditional spectral models, with a global average spatial resolution of 9 km. Its global aerosol forecast system, the Copernicus Atmosphere Monitoring Service (CAMS), is conducted using the same operational model as the NWP driver, but at a lower resolution (40 km or 0.4°) (Benedetti et al., 2009; Eskes et al., 2015; Mangold et al., 2011; Morcrette et al., 2009; Rémy et al., 2019). The China Meteorological Administration (CMA) recently upgraded its forecasting system to a spatial resolution of 12.5 km (J. Zhang et al., 2023). Its aerosol forecast system, the China Meteorological Administration Unified Atmospheric Chemistry Environment (CUACE), includes two versions: the earlier version, driven by the WRF model with an 18-km resolution, and the updated version, driven by the CMA-MESO model, incorporates chemistry-weather interactions with a 10-km resolution. Both versions are regional models (Liu et al., 2022; H. Wang et al., 2022; L. Zhang et al., 2021). WMO recognizes two Regional Specialized Meteorological Centers for sandstorm prediction: Barcelona and Beijing. Both centers provide regional dust forecasts using individual models and multi-model ensembles. The forecast lead times vary, with up to 72 hr for the Barcelona dust center (Terradellas, 2022) and 120 hr for the Beijing center (<http://www.asdf-bj.net>; last accessed on 2024-10-05). As far as we know, these dust forecast services provide little support to renewable energy sectors compared to their NWP counterparts, possibly due to limited resolution or timeliness.

Compared to traditional numerical weather prediction (NWP), the relatively expensive computational load associated with aerosol calculations compels the use of lower resolution and delayed forecasting for dust prediction. CAMS' early development noted that its computational load was twice that of IFS (Mangold et al., 2011). With new algorithms covering more chemical reactions, its complexity grows much faster than numerical weather models, making its resource consumption even more expensive relative to NWP. This development paradigm has two impacts on the renewable energy industry. First, insufficient resolution reduces the ability to forecast extreme events, leading to unforeseen disruptions in power grid operations and causing significant losses. Second, the “near-real-time” dust forecasting approach, that is, integrating calculations after operational NWP, may not align with the power grid's timeliness requirements for reporting power generation plans. Therefore, developing a high-resolution and computationally efficient dust forecast model is worthwhile considering the industry's total value and the significant economic and environmental impacts. Hollingsworth et al. (2008) and Schroedter-Homscheidt et al. (2013) both called for incorporating aerosols into the NWP to enhance weather forecast skills and better serve renewable energy sectors. However, state-of-the-science global dust models have a high level of uncertainty in dust simulations (Huneeus et al., 2011; Textor et al., 2007) and need more research investment in extreme dust storm modeling capabilities at small to medium spatial and temporal scales.

This study aims to design a real-time dust forecast by integrating the dust processes directly into the dynamical core, avoiding significant increases in computational demands and offering advantages over current weather-aerosol-separated solutions. This approach has several benefits. First, the atmospheric processes related to dust are less complex than other aerosols, making it feasible to extract the dust modules from a chemical module, directly integrate them into the dynamical core, and leverage the highly efficient 3D interactions with atmospheric dynamics. Second, weather forecasting models often have higher resolutions than chemistry-aerosol models, enabling better simulation of strong wind processes closely associated with dust and more effectively improving the forecasting skills for extreme dust storm events. Third, higher resolutions and more frequent dynamical update frequencies reduce the unresolved scales in dust-related processes, significantly decreasing uncertainties and simplifying the parameterization process to enhance computational efficiency. Compromises are made by not recognizing dust in-cloud removal processes, dust transport by sub-grid vertical convections within convective clouds, and by simplifying the wet deposition. By leveraging a mature and efficient high-resolution weather

forecasting model, this work reconstructs the fundamental mechanisms of dust generation and settling processes, directly incorporating them into the dynamical core. Compared to a traditional full-fledged Aerosol/Chemistry General Circulation Model (GCM), this dust-only approach is significantly more cost-effective. Consequently, it enables higher resolution and efficient performance within the flagship NWP, providing high-resolution dust storm forecasts with longer lead times. This approach could also benefit the renewable energy industries by offering earlier forecasts compared to existing solutions.

This work is organized as follows: Section 2 provides an overview of the algorithms for integrating the dust processes into the dynamical core. Section 3 discusses the verification strategies. Section 4 demonstrates the results. Finally, Section 5 concludes the main findings and discussions.

2. Algorithms

2.1. The Hosting NWP System

The intricate multiscale characteristics and substantial influence of dynamic transport in extreme dust events necessitate a dynamical core that exhibits adaptability to multiscale weather processes (Morcrette et al., 2009; Pu & Ginoux, 2016). The Finite-Volume Cubed-Sphere Dynamical Core (FV3, <https://www.gfdl.noaa.gov/fv3>; last accessed on 2024-12-19) stands out as a dynamic engine extensively employed in meteorological, climatic, and aerosol transport applications. Its notable efficiency and accuracy make it a suitable candidate for the global prediction of severe dust storms. In most weather scales associated with dust processes, where vorticity motion components dominate over divergence, FV3 ensures absolute vorticity conservation while providing direct forecasts of wind vectors (Lin, 2004). This capability will likely enhance the accuracy of simulating dust transport and other critical processes. The tracer transport scheme (Lin & Rood, 1996) can achieve high order in multiple dimensions, essential for maintaining accurate dispersive properties at very short wavelengths (X. Chen et al., 2018). This capability is particularly beneficial for simulating small-scale severe dust storms.

Furthermore, as spatial resolutions increase, non-hydrostatic dynamics become crucial for accurately depicting local to mesoscale motions, particularly in providing precise representations of intense vertical motions during extreme events. FV3 employs a unique vertical Lagrangian coordinate system, consistently integrating algorithms for both hydrostatic and non-hydrostatic modes, resulting in adept and precise performance (X. Chen et al., 2013; Lin, 2004). Moreover, aerosol transport can utilize longer time steps in the vertical Lagrangian coordinate system, enhancing computational efficiency.

Several influential global tracer transport applications have adopted FV3 as their new dynamical engine, transitioning from the lat-lon version (Lin, 2004) that served as their default dynamical core. These applications include NOAA's Geophysical Fluid Dynamics Laboratory (GFDL) AM4.1/AM3/FLOR dust applications (Horowitz et al., 2020; Paulot et al., 2016; Pu et al., 2019), NASA Goddard Earth Observing System Model and products suite (GEOS/GEOS-Chem/MERRA2; Colarco et al., 2010, 2014), and National Center for Atmospheric Research (NCAR) Community Earth System Model (CESM; Danabasoglu et al., 2020; Gent et al., 2011). The adoption of FV3 by these prominent applications highlights its capability and versatility as the dynamical core for this study.

The GFDL's System for High-resolution prediction on Earth-to-Local Domains (SHIELD; Harris et al., 2020) is a global high-resolution forecasting system built around the non-hydrostatic FV3, with its physical parameterization framework evolving from GFS. This system is particularly well-suited for dust-related applications with multiscale characteristics. SHIELD can quickly achieve variable-resolution computational grids with global coverage through stretching and nesting (Harris & Lin, 2014; Zhou et al., 2019). While ensuring long-term large-scale predictability of dust forecasts, it effectively enhances the simulation's precision, enabling early predictions of extreme dust storm events. This baseline study focuses on a global configuration of 12.5 km, consistent with NCEP GFS and exceeding the resolution of most global dust forecast models. The findings obtained through SHIELD can be smoothly applied to other global models based on FV3. Table 1 lists the main physical parameterization components of SHIELD.

Table 1
SHiELD Main Physical Parameterization Components

Component name	Schemes and references
Convection	Scale-aware simplified Arakawa-Schubert (SAS; Han & Pan, 2011; Han et al., 2017)
Planet Boundary Layer	Eddy-diffusivity mass-flux (EDMF) scheme (J. A. Zhang et al., 2015; Han et al., 2016); Yonsei University boundary-layer scheme (YSU; Hong, 2010)
Radiative transfer	Long-wave and short-wave rapid radiative transfer models (RRTM; Clough et al., 2005)
Cloud microphysics	GFDL cloud microphysics (Zhou et al., 2019)
Cloud fraction	Xu and Randall (1996)
Ozone	Navy's simplified ozone scheme (McCormack et al., 2006)
Terrain induced drags	GFS orographic gravity wave drag and mountain blocking schemes (Alpert, 2004)
Convective gravity wave drag	Chun and Baik (1998)
Land surface model	Noah Land surface model (Ek et al., 2003)
Ocean model	Mixed layer ocean (De Boyer Montégut et al., 2004; Pollard et al., 1973; Thiébaux et al., 2003)

2.2. The Integrated Dust Algorithms

The initial development of global aerosol transport models for atmospheric chemistry impact studies typically begins with relatively inexpensive dust modules. However, as these models become more sophisticated, computational costs increase significantly, forcing aerosol models to run independently from the GCM at lower resolutions. Separating the aerosol model's integration from the GCM and using lower resolutions is a particularly critical issue in industrial applications, as it can lead to less accurate and less timely predictions, hindering effective decision-making in sectors reliant on precise and timely dust storm forecasts, such as renewable energy.

To address this problem, the integrated-dust-dynamics paradigm, hereafter referred to as “iDust” (X. Chen et al., 2024), efficiently integrates dust and weather forecasting by directly incorporating dust emission and removal processes into the dynamical core. All dust module calculations are performed at the tracer transport time level and are at the native Lagrangian model layers, with no exposure to traditional physical parameterization modules. iDust minimizes the overhead between dust calculations and driving dynamics, allowing dust modules to share the dynamical core's current and potential computational optimizations, such as GPU acceleration. By enhancing dust simulation resolution, iDust reduces uncertainties through improved transport precision and more realistic processes like non-hydrostatic dynamics. Additionally, unlike offline modeling driven by externally provided winds or traditional models relying on physics parameterization interfaces, iDust exhibits significantly higher temporal accuracy for dust-dynamics updates. This reduces dependency on PBL mixing, resulting in more realistic emissions and deposition.

As a first step toward developing a high-resolution industrial dust forecast service model, this work focuses on capturing extreme dust storm events, which can seriously impact solar power yields and significantly disrupt power grid functioning. In this initial stage, the online influences of dust on radiative balance and cloud microphysics are not considered to minimize dust-related calculations. However, these processes are crucial for a comprehensive dust forecast model and will be the primary targets of future work.

The essential dust-related modules are described below.

2.2.1. Dust Emission

Dust wind erosion is primarily caused by saltation bombardment (Shao et al., 1993; Tegen & Fung, 1994). Early wind tunnel experiments established that dust uplift at the surface is proportional to the cubic power of the wind speed (Gillette & Passi, 1988; Shao et al., 1993) and is modulated by a wind erosion threshold velocity u_t . A generic dust emission strategy can be summarized in the following form:

$$F_p = CSs_p u_{10}^3 \left[1 - \left(\frac{u_t}{u_{10}} \right)^{n_t} \right], \text{ if } u_{10} > u_t, \quad (1)$$

where F_p is the upward dust flux at the surface of particle size class p , C is the dimensional factor with a wide variation among models (e.g., $1.5 \mu\text{gs}^2/\text{m}^5$ in Takemura et al. (2000); $0.375 \mu\text{gs}^2/\text{m}^5$ in Colarco et al. (2010) and Lu et al. (2016)) and this work uses $0.375 \mu\text{gs}^2/\text{m}^5$, S is the dust source function (Ginoux et al., 2001). Note that this work utilizes a one-degree low-resolution source function to establish a baseline, with fine-scale dust features primarily generated from the high-resolution wind structures. At this initial stage, complex land surface interactions, such as dynamic vegetation and snow cover impacts, are not considered. s_p is the fraction of each dust size class: [0.05, 0.15, 0.3, 0.27, 0.23] for five size bins separated by the particle radius between: [0.1, 1, 2, 3, 6, 10] μm , u_{10} is the horizontal wind speed at 10 m. The threshold velocity u_t is set to 6.5 m/s, based on the reference values from Ginoux et al. (2001) and Takemura et al. (2000). The parameter n_t is a modulating exponent that regulates the relative wind-blasting strength across different wind speeds. Many models chose $n_t = 1$ (Morcrette et al., 2009; Takemura et al., 2000, 2009), a few models use $n_t = 2$ (e.g., the BSC-DREAM model, described in Nickovic et al. (2001), Greed et al. (2008), and Basart et al. (2012)), and some models added a factor of $(1 + u_t/u_{10})$ to blend in some high-order effect of the relative wind strength of u_{10}/u_t (e.g., the MetOffice Unified Model, described in Woodward (2001) and Johnson et al. (2011)). However, due to the considerable uncertainty of wind speed forecast skills, the fine-grained effect of n_t should be determined after the strong wind forecast is well-calibrated. This study uses $n_t = 1$ and reserves it to be determined a posteriori in operational practices. Although not implemented in this work, anthropogenic dust emissions can be important in many applications (Ginoux, Clarisse, et al., 2012; Ginoux, Prospero, et al., 2012; Ginoux et al., 2010) and will be explored in future work.

Most parameters of the emission parameterization are consistent with the GFDL AM4.1 implementation of Georgia Tech/Goddard Global Ozone Chemistry Aerosol Radiation and Transport model (GOCART; Chin et al., 2000, 2002; Ginoux et al., 2001). The dust module in GOCART has been widely implemented in various global and regional climate and weather applications, including NASA GEOS 4/5 (Buchard et al., 2017; Gelaro et al., 2017; Randles et al., 2017), ECMWF CAMS (Morcrette et al., 2009), NOAA NGAC (now GEFS-Aerosol; Lu et al., 2016; J. Wang et al., 2018), and WRF-Chem (Ukhov et al., 2021). In particular, FV3 and its tracer transport algorithm drive most of these models with excellent performance, laying a solid foundation for this work.

2.2.2. Dust Removal Processes

The dust dry removal processes include sedimentation and surface dry deposition. The gravitational settling or sedimentation is the primary removal process for large aerosols. For dust aerosol concentration q_{du} , the change in concentration due to settling is given by Morcrette et al. (2009):

$$\frac{d\rho q_{\text{du}}}{dt} = \frac{d\rho q_{\text{du}} v_g}{dz}, \quad (2)$$

where ρ is the air density, v_g is the sedimentation velocity, given by Stokes law:

$$v_g = \frac{2\rho_{\text{du}} g}{9\mu} r^2 C_{\text{Cunn}}, \quad (3)$$

where ρ_{du} is the dust density for each size bin: [2500, 2650, 2650, 2650, 2650] kg/m^3 , $g = 9.80665 \text{ m}/\text{s}^2$ is the gravitational acceleration. μ is the absolute viscosity coefficient of air:

$$\mu = 1.458 \times 10^{-6} T^{1.5} / (T + 110.4), \quad (4)$$

where T is the temperature, C_{Cunn} is the Cunningham slip-flow correction for small particles:

$$C_{\text{Cunn}} = 1 + \frac{\lambda}{r} \left(1.257 + 0.4 \exp\left(-1.1 \frac{r}{\lambda}\right) \right), \quad (5)$$

where λ is the mean molecular free path of air:

$$\lambda = 6.6 \times 10^{-8} \frac{T}{293.15} \frac{p_0}{p}, \quad (6)$$

where p is the pressure and $p_0 = 101325\text{Pa}$.

A stable numerical discretization for particle settling “implicit fall” is used. At any given layer k (increments in top-down direction), the numerical expression of the settling process is given by:

$$\frac{q_k^{n+1} - q_k^n}{\Delta t} = \frac{1}{\rho_k} \frac{\rho_{k-1} v_{k-1} q_{k-1}^{n+1} - \rho_k v_k q_k^{n+1}}{\Delta z_k}, \quad (7)$$

or

$$q_k^{n+1} = \frac{q_k^n + \frac{v_{k-1} \Delta t}{\Delta z_k} \frac{\rho_{k-1}}{\rho_k} q_{k-1}^{n+1}}{1 + \frac{v_k \Delta t}{\Delta z_k}}, \quad (8)$$

which is solved from a top-down direction with top-level values by:

$$q_1^{n+1} = \frac{q_1^n}{1 + \frac{v_1 \Delta t}{\Delta z_1}}. \quad (9)$$

The subscription “du” is omitted for conciseness. This implicit-fall sedimentation algorithm is adopted from FV3. Morcrette et al. (2009) mentioned that Tompkins (2005) also formed this equation, except equal vertical spacing is assumed.

The surface dry deposition removes aerosols from the bottom of the lowermost model layer as a dry deposition flux (Gallagher et al., 2002; Reddy et al., 2005; Wesely & Hicks, 2000):

$$F_{\text{DD}} = \rho q v_d, \quad (10)$$

where v_d is the dry deposition velocity, expressed in the form:

$$v_d = v_g + \frac{1}{r_a + r_s}, \quad (11)$$

where v_g is the sedimentation velocity given in Equation 3, r_a is the aerodynamic resistance due to turbulent transport to the surface:

$$r_a = \frac{u_{\text{bot}}}{u_*^2}, \quad (12)$$

with u_* the local friction velocity, u_{bot} the horizontal wind speed at the model bottom layer; r_s is the surface resistance to uptake:

$$r_s = \frac{C_b}{u_*}, \quad (13)$$

with $C_b = 100$ is the normalized surface total resistance coefficient for all five dust size bins.

Table 2
Data Sets Used in This Work

Variable	Data set	Resolution		Reference
		Temporal	Spatial (lon × lat)	
PM10	CNEMC	Hourly	Station	CNEMC (2023)
PM10	MITECO	Hourly	Station	MITECO (2022)
10-m wind	CMA	Hourly	Station	CMDC (2023)
532 nm attenuated backscatter coefficient and dust extinction coefficient	AD-Net	15 Min	Station	Shimizu et al. (2004), Sugimoto et al. (2008), AD-Net (2023)
SWD	BSRN	1 Min	Station	Driemel et al. (2018), Baika and Saanouné (2022)
AOD	AERONET	5 Min	Station	Holben et al. (1998, 2001), AERONET (2020)
AOD	Terra-MODIS, Aqua-MODIS, SNPP-VIIRS, NOAA20-VIIRS	Daily	1° × 1°	Platnick et al. (2017a, 2017b), VIIRS Atmosphere Science Team (2023a, 2023b)
Dust RGB images	MSG15-HRSEVIRI	15 Min	1 km	Banks and Brindley (2013), EUMETSAT (2022)
Vertical feature mask, 532 nm total attenuated backscatter	CALIPSO	Daily	Varying	NASA/LARC/SD/ASDC (2023a, 2023b)
Dust mixing ratio, 10-m wind, temperature, pressure, height	MERRA2	3-Hourly, Monthly	0.625° × 0.5°	Global Modeling and Assimilation Office (2015a, 2015b, 2015c), Gelaro et al. (2017)
Dust mixing ratio, DOD, wind, temperature, geopotential	CAMS	3-Hourly, Monthly	0.4° × 0.4°	Benedetti et al. (2009), Morcrette et al. (2009), Peuch et al. (2022), ECMWF (2023)
10-m wind, SWD, TISR	ERA5	Hourly	0.25° × 0.25°	Hersbach et al. (2020), Copernicus Climate Change Service (C3S) (2023)

The wet deposition primarily focuses on the precipitation scavenging processes, using a highly simplified first-order removal rate relationship:

$$\frac{dq_{du}}{dt} = -C_w q_{du} q_{precip}, \quad (14)$$

where q_{precip} is the precipitable water mixing ratio, acquired directly from prognostic tracers exposed to the dynamical core, $C_w = 10^4 \text{ hr}^{-1}$ is the scavenging coefficient. Similar simplified implementations can be found in Tegen and Fung (1994), Chin et al. (2000), and Woodward (2001). The next iteration of algorithm development will focus on refining schemes for wet deposition once the overall dust budget is proven reasonable and more relevant observations are available. The following numerical algorithm blends in some implicit flavor to enhance the calculation stability:

$$q_{du}^{n+1} = \frac{q_{du}^n}{1 + C_w q_{precip} \Delta t}. \quad (15)$$

3. Verification Strategies

3.1. Data Description

The data used in this work, including model data and observational data referenced for model validation and comparison, are summarized in Table 2, with further details provided below.

3.1.1. In Situ Observations

In situ observation is the most reliable direct method for monitoring meteorological elements, with the least uncertainty among all observational sources. Furthermore, due to the infrequent nature of extreme meteorological processes, in situ observations inherently offer outstanding temporal integrity. These data enable statistical evaluation of the performance of models for extreme events over extended periods. Consequently, this study employs diverse in situ observational data sources to undertake a comprehensive and multifaceted assessment of the skills for dust storm forecasts across various models.

Hourly average PM₁₀ (particulate matter with an aerodynamic diameter of less than 10 μm) concentration observations are obtained from the air quality monitoring network operated by the China's National Environmental Monitoring Center (CNEMC, 2023) and the Ministry for Ecological Transition and the Demographic Challenge (MITECO, 2022) in Spain. Hourly 10-m wind is produced by the China Meteorological Information Center in the China Meteorological Administration (CMA), obtained from the China Meteorological Data Service Center (CMDC, 2023). The Asian Dust and Aerosol Lidar Observation Network (AD-Net) continuously monitors the vertical profiles of dust and aerosols by employing dual-wavelength polarization Mie scattering lidar at over 20 observation stations in East Asia (AD-Net, 2023; Shimizu et al., 2004; Sugimoto et al., 2008). In this study, the attenuated backscatter coefficient and dust extinction coefficient at 532 nm are used to examine the vertical profile of dust. AERONET (Aerosol Robotic Network) is a collaborative network dedicated to ground-based remote sensing of aerosols and provides a long-term, continuous database for aerosol research (AERONET, 2020; Holben et al., 1998, 2001). This study utilizes level 2.0 (quality-assured) aerosol optical depth (AOD) at 500 nm. The downward short-wave radiation (SWD) observations at Tamanrasset station (Baika & Saanounne, 2022), part of the Baseline Surface Radiation Network (BSRN; Driemel et al., 2018), are used to validate the short-wave radiation estimates from the offline model accounting for dust optical depth (DOD).

3.1.2. Satellite Products

While satellite observations may be less reliable than in situ observations, they effectively address the issue of spatial coverage gaps inherent in in situ observations. Satellite observations enable a better assessment of the spatial distribution characteristics in model forecasts. Therefore, this study utilizes three types of satellite observations to evaluate horizontal distribution and vertical profile features of the model products.

The first type of satellite observation used in this study is the AOD at 550 nm and the Ångström Exponent, which provide an overview of horizontal dust particle column-integrated distributions. Four AOD data sets used in this work are obtained from the Moderate Resolution Imaging Spectroradiometer (MODIS Collection 6.1; MOD08_D3 and MYD08_D3; Platnick et al., 2017a, 2017b; Sayer et al., 2019) aboard the Terra and Aqua satellites and the Visible Infrared Imaging Radiometer Suite (VIIRS; AERDB_D3_VIIRS_SNPP and AERDB_D3_VIIRS_NOAA20; Hsu et al., 2019; VIIRS Atmosphere Science Team, 2023a, 2023b) sensor aboard the Suomi National Polar-Orbiting Partnership (SNPP) and NOAA-20 satellites. Following the methodology of Pu and Ginoux (2018), the AOD is converted to DOD using the Ångström Exponent (α) to filter out small particles:

$$\text{DOD} = \text{AOD} \times (0.98 - 0.5089\alpha + 0.0512\alpha^2). \quad (16)$$

Measurements from these four instruments are further averaged to obtain a daily combined AOD and DOD. The second type of satellite observation is the dust RGB images (EUMETSAT, 2022) from the Meteosat Second Generation (MSG) Spinning Enhanced Visible and Infrared Imager (SEVIRI; Banks & Brindley, 2013). This data set offers atmospheric dust observations every 15 min with a spatial resolution of 1 km, making it highly effective for monitoring and analyzing dust events. The third type of satellite observation includes the vertical profile of the 532 nm total attenuated backscatter (level 1, V4-51) and vertical feature mask (VFM, level 2, V4-51) (NASA/LARC/SD/ASDC, 2023a, 2023b) from the Cloud-Aerosol Lidar and Infrared Pathfinder Satellite Observation (CALIPSO; Winker et al., 2010) Satellite, providing insights into the vertical distribution of dust particles in the atmosphere. By combining these three types of satellite observations, this study aims to comprehensively evaluate the performance of model forecasts in capturing both the horizontal and vertical characteristics of dust events.

Table 3
Essential Dust Modules and Their Key Parameters

Model	Resolution (lon × lat × lev)	Size bins (μm in radius)	Emission scheme	Deposition scheme
iDust	0.1° × 0.1° × 63L	0.1–1.0, 1.0–2.0, 2.0–3.0, 3.0–6.0, 6.0–10.0	Equation 1 with critical parameters: $n_r = 1, u_r = 6.5 \text{ m/s}$	See Equations 10 and 14
MERRA2	0.625° × 0.5° × 72L (Bosilovich et al., 2016)	0.1–1.0, 1.0–1.8, 1.8–3.0, 3.0–6.0, 6.0–10.0 (Collow et al., 2022)	Scheme described in Ginoux et al. (2001). u_r is a function of particle diameter, surface roughness, and other factors	See Colarco et al. (2014)
CAMS	0.4° × 0.4° × 137L (Rémy et al., 2022)	0.03–0.55, 0.55–0.9, 0.9–20 (Rémy et al., 2022)	Adapted from the MB95 Scheme (Marticorena & Bergametti, 1995). u_r depends on factors such as particle size, surface roughness, and soil moisture, among others (Rémy et al., 2022)	See Rémy et al. (2019)

3.1.3. GCM Products

This work benchmarks iDust forecasting results against two extensively used dust GCMs, focusing on extreme dust storms that significantly impact solar energy operations and maintenance. The first benchmark model is NASA's Modern-Era Retrospective analysis for Research and Applications, Version 2 (MERRA2; Gelaro et al., 2017). MERRA2 assimilates aerosol optical depth data from various platforms and captures the three-dimensional evolution of dust aerosols (Buchard et al., 2017; Tindan et al., 2023). This study compares forecast performance using MERRA2 10-m wind (MERRA2 inst1_2d_asm_Nx), dust mixing ratio at the model level (MERRA2 inst3_3d_aer_Nv), and meteorology fields such as pressure, temperature, and height at the model level (MERRA2 inst3_3d_asm_Nv) (Global Modeling and Assimilation Office, 2015a, 2015b, 2015c). iDust also uses MERRA2 as the initial condition in many scenarios. The second benchmark model is the CAMS forecast by ECMWF (Peuch et al., 2022), which integrates satellite-based observations with aerosol chemical models using 4D-VAR data assimilation (Rémy et al., 2022). CAMS (ECMWF, 2023) provides one of the earliest near-real-time (NRT) global aerosol forecast services. This study compares forecast performance using CAMS wind, dust concentration, temperature, and geopotential. A comparison of the dust emission schemes, particle size distributions, deposition schemes, and key parameters for iDust, MERRA2, and CAMS is presented in Table 3. Additionally, ERA5 (Copernicus Climate Change Service (C3S), 2023; Hersbach et al., 2020) by ECMWF serves as a benchmark for evaluating 10-m wind speed predictions and facilitates the analysis of extreme dust event occurrences. ERA5 surface short-wave downward radiation (SWD) and the top-of-atmosphere short-wave radiation (TISR) are also used to calculate the impact of dust on the photovoltaic resource.

The dust optical depth (DOD) in MERRA2 and iDust is derived from the dust mass loading via the relationship below

$$\tau = \sum_{i=1}^5 \epsilon_i M_i \quad (17)$$

where τ is the dust optical depth, M_i is the dust mass loading in each of five dust bins in unit of kg/m^2 , and ϵ_i is the corresponding mass extinction efficiency with values of [2090.9, 499.6, 274.18, 146.59, 78.226] m^2/kg . These mass extinction efficiencies are calculated at 550 nm with a Mie code. The calculations assume spherical particles and constant mass distribution over five bins (0.1–1, 1–2, 2–3, 3–6, and 6–10 μm). A refractive index provided by Balkanski et al. (2007), with 2.7% hematite content, is used. No hygroscopicity of dust particles is assumed.

3.2. Dust Initial Condition

The presence or absence of initial dust conditions in short-term dust forecasts impacts the first few days (Benedetti et al., 2009; Rubin et al., 2016; Sekiyama et al., 2016). Although SHiELD can utilize the analysis fields generated by the Gridpoint Statistical Interpolation (GSI, <https://ral.ucar.edu/solutions/products/gridpoint-statistical-interpolation-gsi>; last accessed on 2024-12-19) Data Assimilation System of GFS for meteorological field forecasting, iDust still requires a dust-specific data assimilation system.

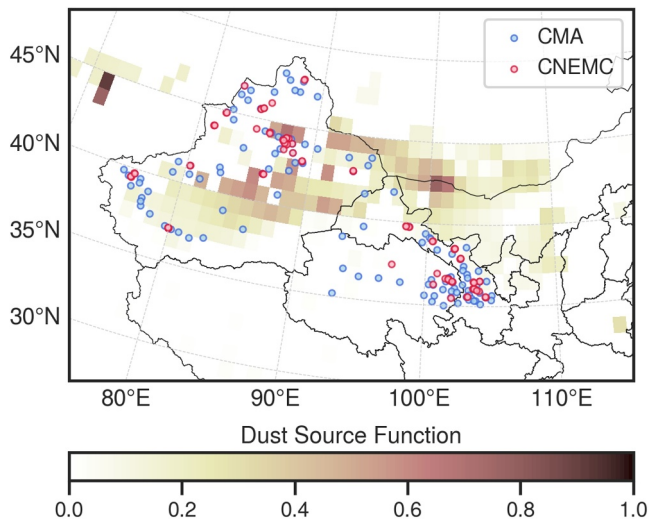


Figure 1. Spatial distribution of dust source function (shading), as well as surrounding 121 CMA (blue points) and 97 CNEMC (red points) observation stations.

However, the dust lifetime is about 3–4 days (Textor et al., 2006), with stronger dust storms dominated by larger particles having even shorter life-cycles. With accurate wind field forecasting, it is possible to simulate the formation and evolution of intense dust storms several days in advance, even without initial dust fields. This approach, similar to the “free-wheeling” mode described by Morcrette et al. (2009) in their study on CAMS, will be evaluated in iDust for its ability to provide early detection of severe storms.

To emulate scenarios with initial dust fields and a data assimilation (DA) enabled workflow, this study employs MERRA2 dust data at analysis model layers as initial dust conditions. A corresponding software interface based on the Flexible Modeling System (FMS, <https://github.com/NOAA-GFDL/FMS>; last accessed on 2024-12-19) has been developed for this purpose. The results with and without initial dust fields will be comprehensively compared to assess the impact of initial conditions on forecasting performance.

3.3. Meteorological Field Evaluations

Accurate wind forecasts are crucial for dust storm prediction. Many online dust models treat the driving GCM as a static foundation, only adjusting dust parameterizations to achieve reasonable global dust climatology. However, this approach introduces significant uncertainties in predicting dust storms

and other low-occurrence extreme events. In particular, crucial parameters, such as the threshold velocity of wind erosion, are derived from field campaigns and wind tunnel experiments. However, models have substantial biases in strong wind events, leading to considerable errors in dust storm prediction if experiment-based parameters are directly applied. Therefore, assessing biases in model wind speed forecasts can help determine the selection of critical parameters in dust emission mechanisms.

This study evaluates surface wind simulation skills among various models against 10-m wind speed observations, emphasizing wind speed biases in dust-prone regions. Data from 121 wind speed stations (CMA) and 97 PM10 aerosol concentration observation stations (CNEMC) in northwestern China are used to examine wind speeds and dust simulations. This region is critical for developing photovoltaic energy in China but is also most affected by dust storms. Figure 1 illustrates the spatial distribution of CMA and CNEMC stations alongside the dust source function of Ginoux et al. (2001). The observational stations cover China’s most arid and semi-arid regions (X. Chen et al., 2007), with minimal impact from anthropogenic industrial emissions. Model results are interpolated to the stations via the bilinear method.

4. Results

4.1. The 2023 Spring Dust Season in Northwest China

China has rapidly expanded its renewable energy sectors in recent years, establishing a leading position in solar energy (Pourasl et al., 2023). Its top solar-producing provinces are in the northwest, significantly affected by the Taklamakan and Gobi Deserts (Global Energy Monitor, <https://globalenergymonitor.org>; last accessed on 2024-02-08). In 2023, dust storm frequency reached a decade-high (S. Chen et al., 2023), severely impacting the renewable energy industry. This section focuses on the dust processes in Northwest China during the spring of 2023. The high occurrence of extreme dust events in this season provides a unique opportunity to draw statistically sound evaluations on dust storm predictions.

Surface wind is the most determining factor in dust emission processes, making it crucial to validate the 10-m wind velocity characteristics between different models (Ortiz & Smolarkiewicz, 2006). Figure 2 presents the evaluation of wind speed simulations from CAMS, ERA5, MERRA2, and iDust in the northwest region of China during the spring of 2023, based on CMA station observations (see Figure 1). The scatter plots illustrate the relationship between 10 m wind speeds simulated by the GCMs and site observations (Figures 2a–2d). The number of measurements (N), correlation coefficient (r), and slope (k) of the fitted linear relations are provided for each model. Figure 2e illustrates the probability density function (PDF) distribution of corresponding samples. All forecast data in the figure are at 25–48 hr lead times.

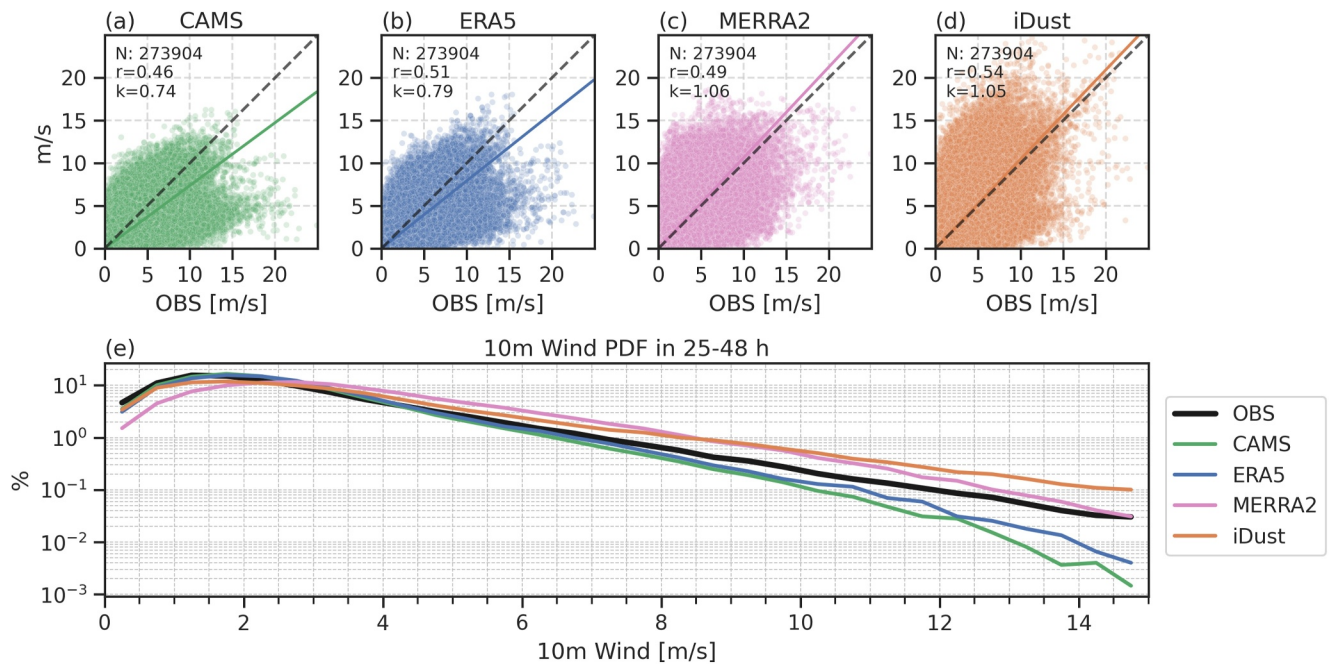


Figure 2. (a–d) Scatter plots between the 10 m wind speed produced by the GCMs and the site observations. The solid lines are obtained using linear least-squares regression with slopes (k). N represents the total number of measurements used to derive linear regressions. The correlation coefficient (r) indicates the consistency between simulations and observations. The black dashed line represents a reference line with a slope of 1. (e) Probability density function (PDF) distribution of all samples. All forecast data in the panels are at 25–48 hr lead times.

The scatter plots (Figures 2a–2d) indicate that CAMS and ERA5 tend to underestimate extreme wind speeds while MERRA2 and iDust have better wind speed simulated values with slight overestimation, judged by the fitted slope values k . CAMS, showing the smallest slope and lowest correlation coefficient, significantly underestimates wind speeds, impairing its ability to accurately simulate extreme dust emissions. Among the models, iDust (or the driving SHIELD) exhibits the best slope and coefficients, particularly in high wind speed regions. The probability density distribution of 10 m wind speeds (Figure 2e) further supports these findings. CAMS and ERA5 accurately simulate wind speeds below 6 m/s but underestimate wind speeds above 6 m/s, with the magnitude of underestimation increasing with wind speed. Conversely, while MERRA2 and iDust slightly overestimate strong wind frequencies, they can simulate extreme winds around dust source regions, which may be beneficial for capturing extreme dust emissions. Analysis at other lead times shows similar results, and the plots are included in Supporting Information S1 (Figure S1). An alternative graded-wind-speed analysis is also performed (see Figure S2 in Supporting Information S1) to further support the above findings. These biases should be taken into consideration during dust emission parameter tuning.

Building upon the wind speed evaluation, Figure 3 evaluates PM10 simulations from CAMS, MERRA2, iDust, and iDust-M2 (iDust initialized by MERRA2 dust fields) in the northwest region of China during the spring of 2023, based on CNEMC sites observations (see Figure 1). Given the significant model underestimation of PM10 when large values appear, the model output for PM10 uses a simple estimation of the total surface dust concentration across all models instead of distinguishing between different size bins. CAMS, with the lowest correlation coefficient and slope, indicates the most significant underestimation of PM10 concentrations (Figure 3a). MERRA2 performs better than CAMS with a slope of 0.47, although it still vastly underestimates PM10 levels (Figure 3b). Interestingly, even without initial dust data, iDust demonstrates improved performance compared to MERRA2 and CAMS (Figure 3c). iDust-M2 achieves the highest slope of 0.65 among the models, including the reanalysis product MERRA2 (Figure 3d). All models, nonetheless, underestimate extreme PM10 events. Analysis at other lead times shows similar results, and the plots are included in Supporting Information S1 (Figure S3). An alternative graded-PM10 analysis is also performed (see Figure S4 in Supporting Information S1) to further support the above findings. According to these results, improvements in extreme wind speed simulations and refined dust parameterization (e.g., localized u_c) may further enhance the model quality and are worth pursuing in the forthcoming explorations.

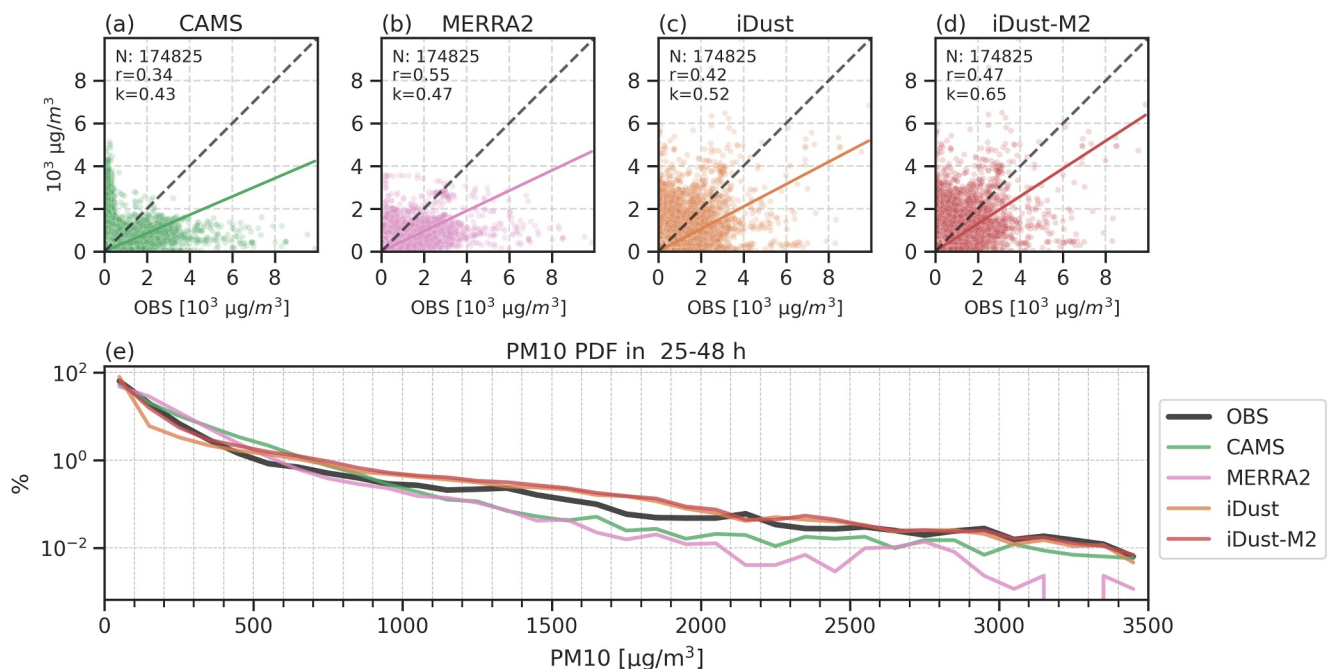


Figure 3. Same as Figure 2, but it shows the intensity of PM10.

The PDF curves reveal that the frequency of extreme dust events with PM10 concentrations exceeding 1000 $\mu\text{g}/\text{m}^3$ is less than 1%. For these high-impact extreme dust events, both CAMS and MERRA2 significantly underestimate their occurrence. In contrast, both iDust and iDust-M2 provide frequencies that closely align with observations, especially for extreme dust events. The improved simulation of hazardous PM10 events is likely due to a better representation of extreme winds at the higher resolutions in iDust. Agustí-Panareda et al. (2019) also reported enhanced tracer simulation capabilities with increased model resolution. Notably, iDust utilizes a threshold wind erosion velocity of 6.5 m/s, while CAMS applies a range from 3.5 m/s over the Taklimakan to 6 m/s over the Sahara (Rémy et al., 2019). Despite CAMS using a significantly lower threshold (≤ 3.5 m/s) in Northwest China, it still underestimates extreme dust events, suggesting that the underestimation of surface wind forecasts in extreme conditions has a more substantial impact.

In situ based validation provides excellent temporal coverage but lacks spatial coverage, especially in inhabitable desert regions. Figure 4 illustrates the spatial distribution of (a) satellite-averaged DOD anomaly, and (b–e) DOD anomalies from MERRA2, CAMS, iDust, and iDust-M2, averaged over 49–72 forecast hours during 2023 spring. Additionally, (f) the RMSE (root mean square error) and (g) the ACC (anomaly correlation coefficient) between the simulation and observation over Inner Mongolia (indicated by the cyan edge line in Figure 4) and Xinjiang (purple edge line) are presented. The climatology is defined as the average from March to May over the period of 2013–2023 except for CAMS. Since CAMS underwent a major upgrade in 2019 (<https://www.ecmwf.int/en/about/media-centre/news/2019/upgrade-improves-global-air-quality-forecasts>; last accessed on 2024-10-05), only DOD from 2020 to 2023 is used to derive the climatology. The satellite observation climatology is calculated using satellite observation. For MERRA2, iDust, and iDust-M2, MERRA2 DOD climatology is used. The use of DOD anomalies instead of DOD to calculate the correlation coefficient is due to significant differences between the DOD climatologies from satellite observations and models (see Figure S5 in Supporting Information S1). This approach reduces the influence of systematic biases and highlights the impacts of unusually high activities of extreme dust events during 2023.

In the Gobi Desert region in Inner Mongolia, where better dispersion conditions are expected, MERRA2 and CAMS significantly underestimate DOD anomaly, while iDust-M2 reasonably simulates the spatial distribution of DOD anomaly with intensities closer to observations. Notably, even without initial conditions, iDust produces strong DOD values in western Inner Mongolia that are closer to observations than those from CAMS and MERRA2. In the Taklamakan Desert region of the Tarim Basin in Xinjiang, iDust-M2 closely aligns with satellite

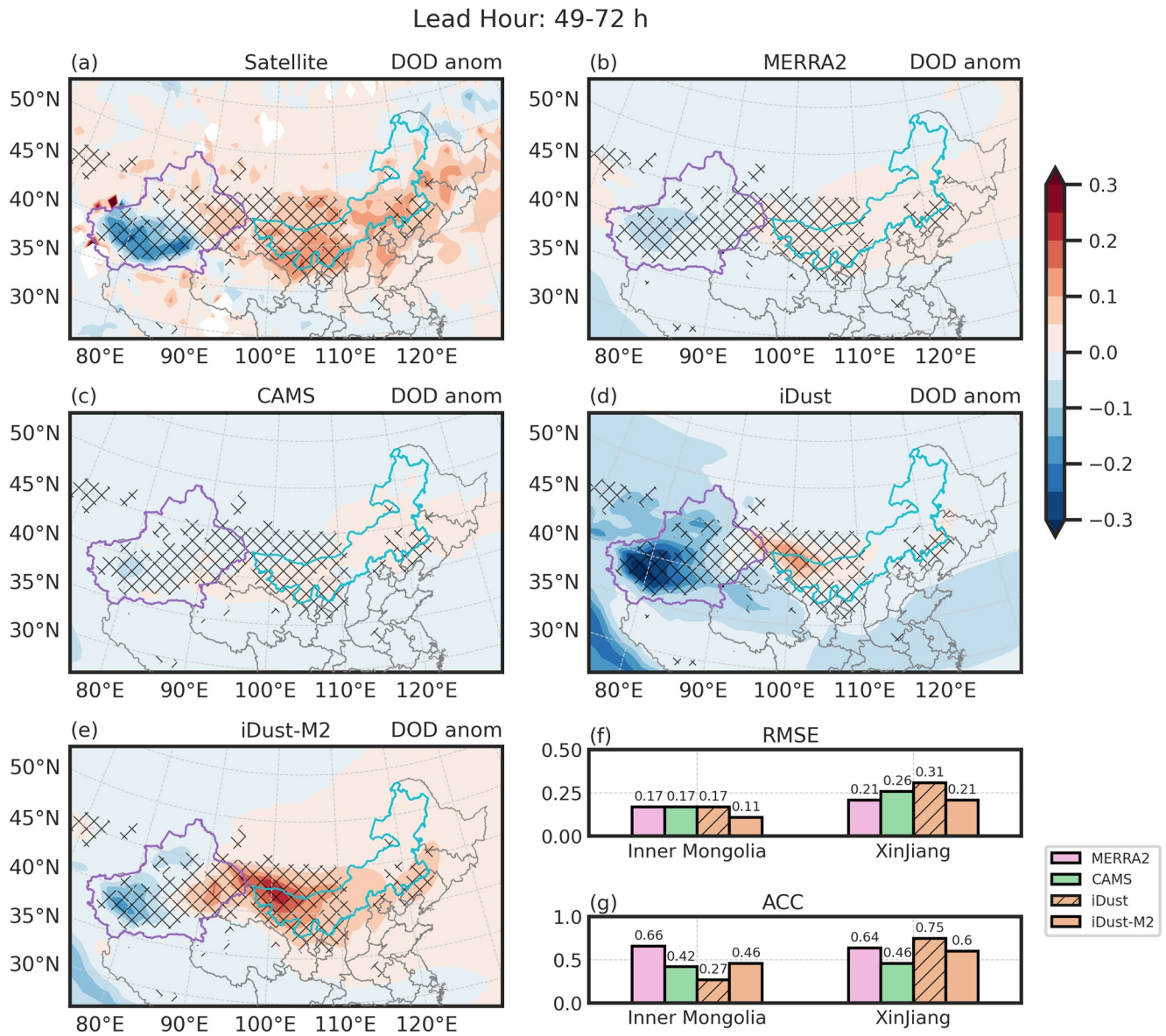


Figure 4. Spatial distribution of (a) MODIS and VIIRS averaged DOD anomaly and (b–e) 49–72 hr forecast averaged DOD anomalies from MERRA2, CAMS, iDust, and iDust-M2 during spring 2023. (f) RMSE and (g) ACC between the simulation and observation over Inner Mongolia and Xinjiang are also presented. Cyan and purple edge lines in panels (a–e) denote Inner Mongolia and Xinjiang, respectively. Hatched areas indicate dust source regions (dust source function > 0.01).

DOD anomaly. The iDust DOD anomaly in this region is lower than observed, likely due to basin topography and poor dispersion conditions, thus, the longer lifetime small dust particles maintain afloat in the air for an extended period. iDust underperforms here because of the lack of dust initial conditions and inadequate representation of background fine particles. Nonetheless, iDust-M2 shows better RMSE and ACC performance than CAMS in both Inner Mongolia and Xinjiang, effectively simulating the average DOD over dust source regions in China during spring 2023, though there remains room for improvement.

Given that solar energy prediction is one of the primary applications of this work, a preliminary dust-affected solar energy resources assessment is conducted. The dust deposition effect is calculated using iDust-M2 dust deposition (DDEP), assuming that the photovoltaic panels are cleaned once at the beginning of each month. Based on Panat and Varanasi (2022), the conversion rate of photovoltaic dust coverage η_d with the panel surface dust deposition M is approximately:

$$\eta_d = \exp(-M/M_0), \quad (18)$$

where $M_0 = 8 \text{ mg/cm}^2$ is read from Panat and Varanasi (2022). For the dust extinction effect, a highly simplified offline model is designed based on hourly DOD data to estimate the unattainable solar energy due to dust extinction in Northwestern China during the spring of 2023. Referring to the study by Antón et al. (2012), the following equation reflects the discrepancies of short-wave downward radiation (SWD) due to DOD:

$$\Delta\text{SWD}_{\text{DOD}} = \text{TISR} \cdot e^{-k\text{DOD}}, \quad (19)$$

where $\Delta\text{SWD}_{\text{DOD}}$ represents the reduction in SWD caused by DOD, and TISR is the top-of-atmosphere (TOA) short-wave downward radiation from ERA5. Using SWD observations from the Tamanrasset station, obtained from the Baseline Surface Radiation Network (BSRN), a fitted coefficient $k = 0.15$ is derived.

Figure 5 presents the spatial distribution of various surface Short-Wave Downward radiation (SWD) metrics in spring 2023 (March, April, and May) based on iDust-M2 forecast data at 97–120 lead hours. Panel (a) shows the ERA5 total SWD, while panel (b) depicts the SWD discounted for the effects of dust deposition on solar panels. Panel (c) illustrates the unattainable solar energy due to dust deposition, and panel (d) focuses on the unattainable solar energy caused by DOD. Panels (e) and (f) depict the proportion of these discrepancies relative to the total short-wave radiation. The calculations in panels (a–f) represent the cumulative values for the spring season. Panels (g) and (h) also show monthly mean dust deposition and the season-mean hourly DOD, respectively. Note that in Figure 5b, we did not subtract the DOD-related unattainable solar energy shown in panel (d), as ERA5 already accounts for the monthly mean climatology of dust (<https://confluence.ecmwf.int/display/FUG/Section+2.1.5.7+Aerosols+and+Greenhouse+Gases>; last accessed on 2024-10-05). An actuarial evaluation of dust-radiative impacts may require online dust-radiative-transfer calculations, which warrants further exploration.

The SWD distribution pattern alters significantly when accounting for dust deposition (Figures 5a and 5b), revealed by a more detailed analysis in Figures 5c–5h. SWD discrepancies from dust deposition are more localized, with higher peak values, as shown in panels (c) and (e). In contrast, SWD discrepancies due to DOD exhibit a more uniform spatial distribution and a broader impact range, as illustrated in panels (d) and (f). The analysis estimates that dust deposition on solar panels in Northwestern China may block more than 100 kWh/m^2 of shortwave downward radiation (Figure 5c), causing unattainable solar energy surpassing 25% in some areas (Figure 5e), which is highly significant for the photovoltaic industry. A more detailed assessment of photovoltaic resources can be conducted in future work.

The above studies demonstrate iDust's overall performance in simulating and predicting dust events during spring 2023 in Northwestern China. To further illustrate iDust's capability in capturing the evolution and intensity of extreme dust events, in the following case studies of significant dust events, all iDust simulations are initialized with MERRA2 dust initial conditions and labeled iDust for brevity. A case study is presented on an extended dust episode that took place on April 10th and 12th–13th in 2023. Figure 6 depicts the satellite-observed DOD on April 9th and the CALIPSO track around 20:35 UTC (orange line), along with the location of an AD-Net site Sainshand (black circle) used in Figure 7. CALIPSO's observations of aerosol subtype vertical distribution and backscatter signal at 532 nm show that the dust plume with the highest concentration is between 40°N and 45°N , reaching above 6 km. All three numerical products exhibit intense aerosol concentrations. Notably, iDust is the only model that exhibits the observed high vertical dust uplift, closely matching the observation, which is also anticipated with the numerical properties of high-resolution dynamics.

Figure 7 shows the vertical profiles of the observed 532 nm backscatter coefficient, dust extinction coefficient at the AD-Net station Sainshand (44.87°N , 110.12°E), and the dust concentration from MERRA2 reanalysis, CAMS, and iDust. A conversion from dust concentration to the dust extinction coefficient is also possible to calculate, and the corresponding comparisons are included in Supporting Information S1 (Figure S6). However, due to significant size bin differences between the models and the sensitivity of key parameters in the conversion algorithms, the direct comparisons of dust extinction coefficients may have large uncertainties. Observations reveal significant near-surface dust concentration increases between April 8th and 10th, with the highest concentration near the surface on April 9th and at higher altitudes on April 10th. On April 12th and 13th, a high-altitude dust plume above 6 km is observed, indicating upper-atmosphere dust transport (Figures 7a and 7b).

Lead Hour: 97-120 h

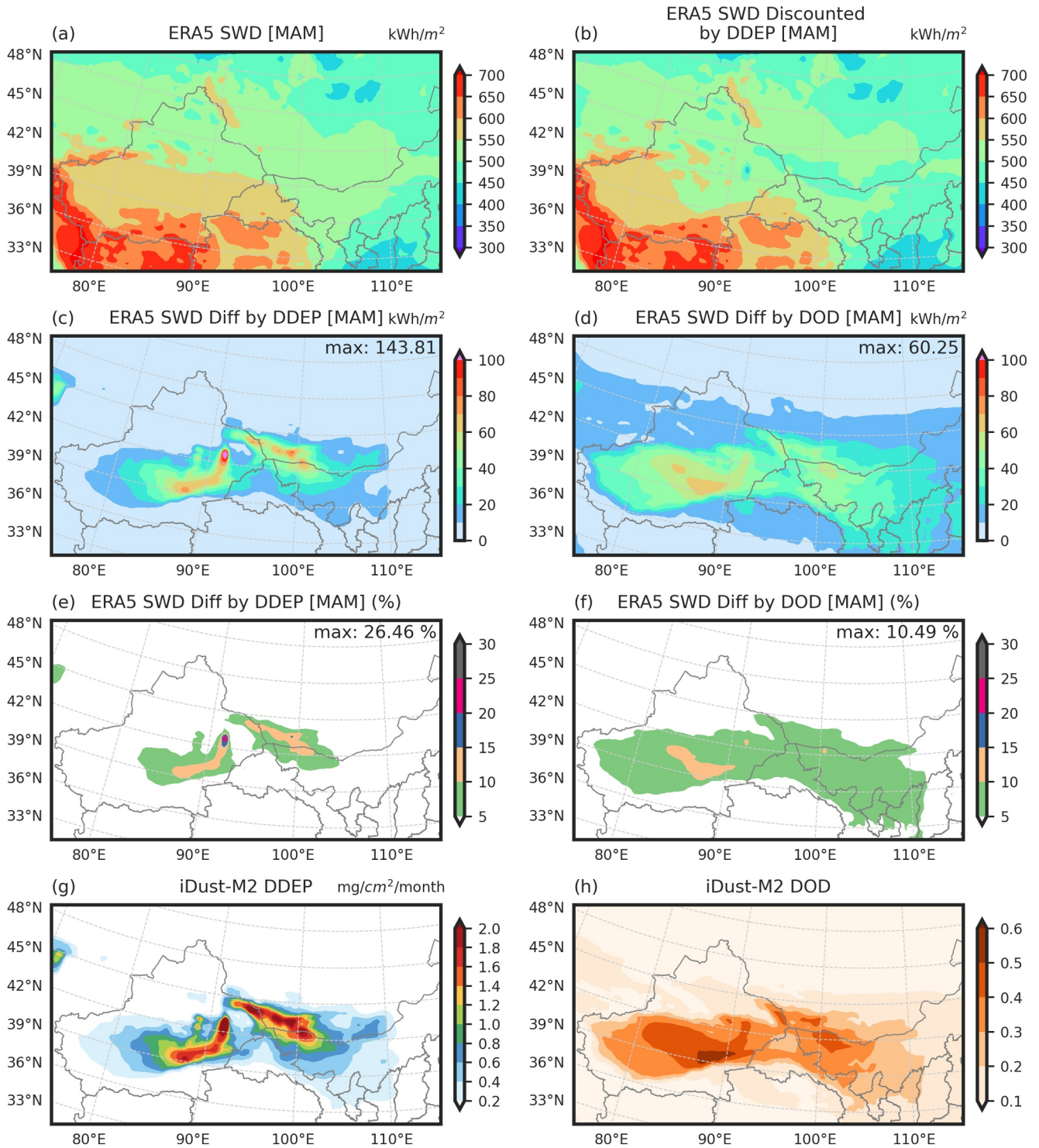


Figure 5. The spatial distribution of surface (a) ERA5 shortwave downward radiation (SWD), (b) ERA5 SWD discounted by the dust deposition on the solar panels, (c) the SWD discrepancies due to the dust deposition on the solar panels, (d) the SWD discrepancies due to the DOD, (e and f) the proportion of unattainable solar energy relative to the total short-wave radiation, (g) the monthly mean dust deposition, and (h) season-mean hourly DOD. The figure is based on iDust-M2 forecast data at 97–120 lead hours. Maximum values are displayed in the upper right corner of each panel for (c–f).

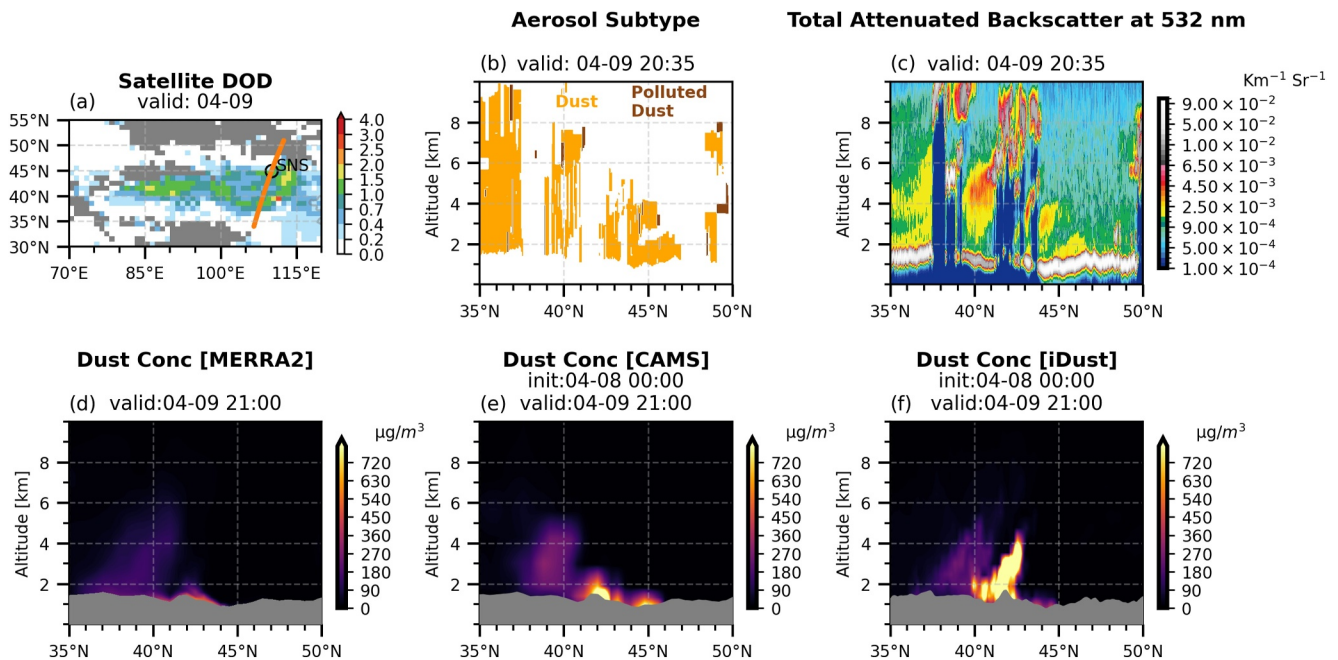


Figure 6. (a) Satellite-observed DOD with gray shading showing the missing values. The circle indicates the location of the AD-Net station Sainshand used in Figure 7. The orange line represents the CALIPSO track. (b) Aerosol Subtype and (c) total attenuated backscatter at 532 nm observed by CALIPSO. In (d–f), dust concentrations along the CALIPSO track are shown for MERRA2, CAMS, and iDust. The gray shading represents topography.

While all models capture the high near-surface dust concentration between April 8th and 10th, MERRA2 underestimates upper-level dust concentration on April 12th and 13th. CAMS fails to capture the dust transport occurring at high altitudes on April 13th. iDust simulation shows high consistency with observations in the vertical distribution and temporal dust changes during this process. It is the only model among the three that successfully simulates intense dust concentration at high altitudes. In this extreme dust episode, iDust demonstrates higher capabilities in simulating the vertical distribution and long-distance dust transport compared to CAMS and MERRA2 reanalysis, making it a valuable tool for forecasting the long-range transport of dust storms and understanding their impact on the environment, air quality, and affected infrastructures.

4.2. The Northward Long-Range Transport to European Dust Storm in March 2022

During 14–17 March 2022, Saharan dust outbreaks, extending from North Africa to the Iberian Peninsula, were characterized by historic intensity and duration, making it an excellent case for testing dust prediction models. The event led to record-breaking PM₁₀ concentrations at 107 out of 471 stations in Spain, with the highest exceeding $1,700 \mu\text{g}/\text{m}^3$ (Liger et al., 2024; Micheli et al., 2024). The extreme nature of this event, with its narrow transport passage, high intensity, and extensive distance covered, poses significant challenges to model performance. A deep low-pressure system west of the Iberian Peninsula and a persistent high-pressure system in southern Europe facilitated the formation of an efficient, elongated corridor of intense dust transport resembling a narrow “river” (Chakraborty et al., 2022; Hu et al., 2022; Lapere et al., 2024). A comprehensive verification analysis of this event is presented as follows.

Figure 8 shows the spatial distribution and time series of PM₁₀ across Spain during the March 2022 Saharan dust outbreak. Panels (a–d) depict the daily averaged PM₁₀ spatial distribution on March 15th from ground observations, MERRA2 reanalysis, CAMS, and iDust, respectively, with cyan, purple, and green circles representing stations in Jaén, Madrid, and Valladolid. The RMSE and Pearson correlation coefficients are provided below each panel. Observations show the most severe deterioration in air quality over mainland Spain occurs on the 15th, with dust propagating from southeast to northwest. MERRA2 aligns with observations in PM₁₀ intensity but overestimates the extent of the affected area and PM₁₀ concentration over northwestern Spain, and fails to simulate the PM₁₀ peak over central and southeastern Spain. CAMS significantly underestimates the dust concentration on the 15th, while iDust’s forecasted PM₁₀ intensity and spatial distribution are most consistent with observations

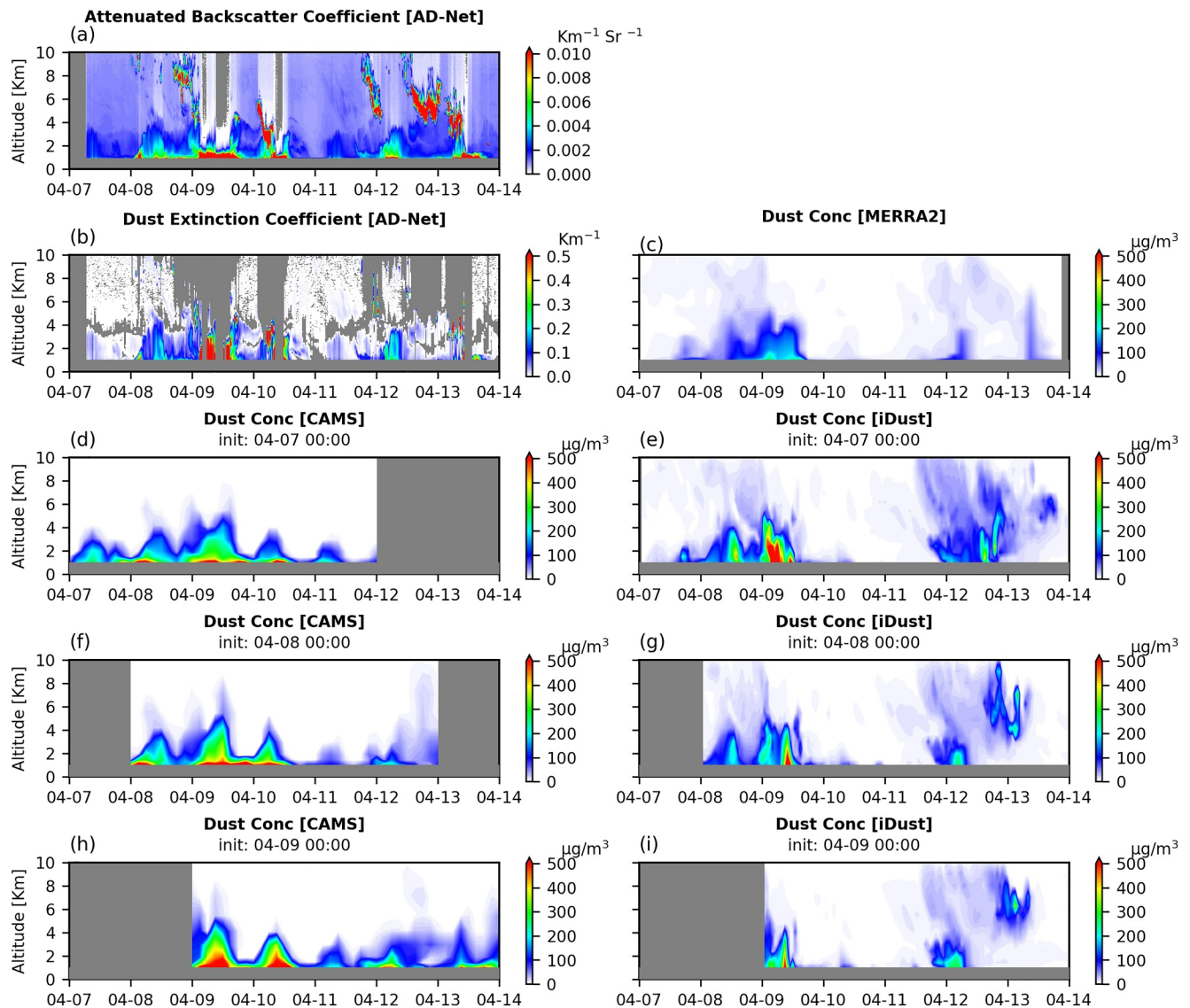


Figure 7. Vertical profiles of observed (a) 532 nm backscatter coefficient and (b) dust extinction coefficient at the AD-Net station Sainshand, along with dust concentration simulated by (c) MERRA2 reanalysis, (d, f, h) CAMS, and (e, g, i) iDust. Simulations initialized at different times are shown for CAMS and iDust. The gray color in each panel indicates missing values.

and show the best RMSE and correlation coefficient. Underpredicted dust concentrations are somewhat revealed by the PM10 time series for Jaén, Madrid, and Valladolid (Figures 8e–8g), while CAMS displays more flattened PM10 levels in these provinces. iDust outperforms CAMS in terms of RMSE (R) and correlation coefficient (C) in most validation comparisons.

Satellite-observed and model-simulated DOD at noon on March 15th and 16th, shown in Figure 9, provide a continuous spatial perspective to assess model performances during this intense dust episode. On March 15th, both reanalysis and forecast models capture significant dust concentrations over the northwest Iberian Peninsula, but CAMS simulates a different DOD structure in North Africa compared to observations. On March 16th, cyclonic circulation transports dust southward to the northwest coast of Africa. CAMS, which underestimates DOD intensity and spatial extent, fails to simulate such a feature. iDust and MERRA2 show better dust transport patterns, with iDust aligning more closely with observations. RMSE and correlation coefficient of iDust are close to those of MERRA2, and marginally better than CAMS. iDust also simulates detailed dust structures that align well with satellite observations.

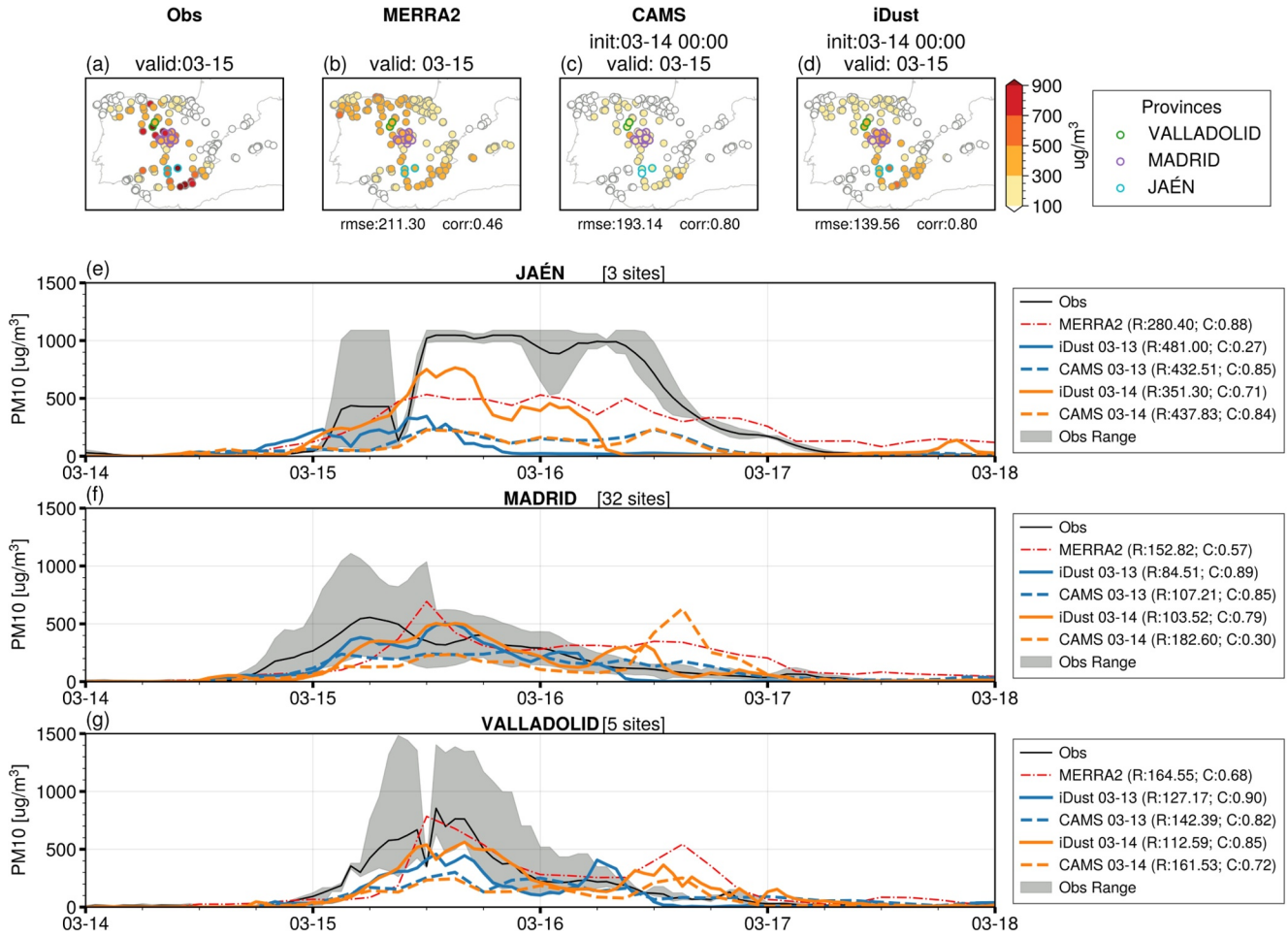


Figure 8. Spatial distribution and time series of PM10 over Spain during the March 2022 Saharan dust outbreak. Panels (a–d) show the daily averaged PM10 concentrations on March 15th from (a) observations, (b) MERRA2, (c) CAMS, and (d) iDust. Circles indicate monitoring stations located in Jaén (cyan), Madrid (purple), and Valladolid (green). RMSE and Pearson correlation coefficient for each data set are provided below each panel. Panels (e–g) present the time series of PM10 averaged over the stations in Jaén, Madrid, and Valladolid, respectively, with the RMSE (R) and correlation coefficient (C) shown in the legend.

iDust's high-resolution dynamics offer direct prognostic vertical motions on small scales, potentially providing simulation advantages in extreme cases, which are highly associated with convective conditions. Figure 10 illustrates the time-series and key-frame spatial distribution of dynamic properties during this event by comparing the vertical and horizontal movements and vertical dust flux between the two models. The vertical velocity of CAMS is approximated using the equation:

$$w = -\frac{RT}{Pg} \cdot \omega, \quad (20)$$

where w is the vertical velocity, $R = 287.058 \text{ J/kg/K}$ is the ideal gas constant, T is the temperature, P is the pressure, g is the gravity acceleration, and ω is the pressure vertical velocity. The horizontal and vertical kinetic energy partitions (K_h and K_v) are calculated as:

$$K_h = \frac{1}{2}\rho_a(u^2 + v^2), K_v = \frac{1}{2}\rho_a w^2, \quad (21)$$

where ρ_a is the air density, u and v are the horizontal wind components. Finally, vertical dust flux F is calculated using:

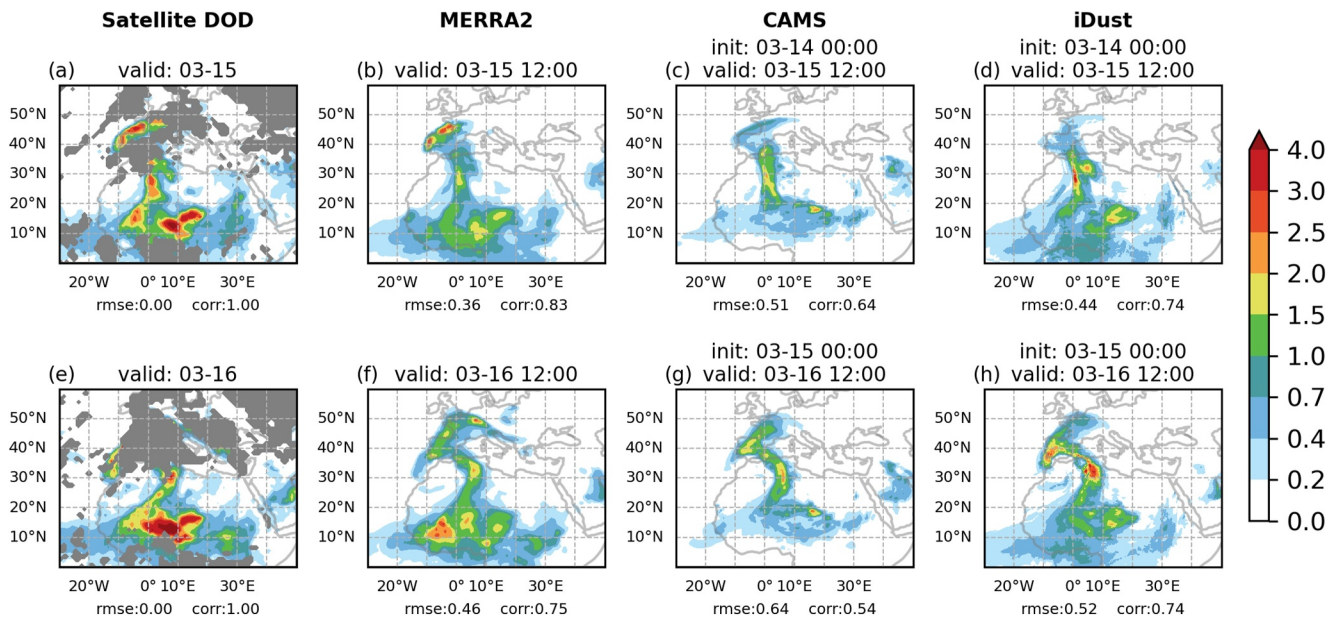


Figure 9. The spatial distribution of satellite-observed DOD and simulated DOD by MERRA2, CAMS, and iDust, with RMSE and correlation coefficient shown below each panel. The first and second rows show results validated on March 15th and 16th, respectively.

$$F = q_{du} \cdot w \quad (22)$$

where q_{du} is the dust concentration in kg/m^3 . Both iDust and CAMS initiated their forecasts at 00:00 on 14 March 2022. All spatial distributions presented in the figure correspond to 00:00 on 16 March 2022, as indicated by the green lines in panels (d, g, j). The time series panels show the average values for the region marked by the red box in the spatial distribution maps, computed after remapping to a 0.4-degree resolution.

Both CAMS and iDust exhibit large-scale DOD distributions similar to the observations, with iDust showing a more pronounced rotational pattern with stronger and more concentrated DOD distribution (Figures 10a–10c). Figures 10d–10f compare the time evolution and spatial distribution in vertical velocity, revealing stronger vertical activity in iDust compared to CAMS, especially during the key dust transportation period. On the other hand, Figures 10g–10i compare the horizontal velocity. Although the overall magnitudes of horizontal kinetic energy partitions are similar between the two models, iDust shows slightly stronger horizontal winds in dust-affected areas, likely due to the higher model resolution. Lastly, Figures 10j–10l examine the vertical dust transport activities. As shown in panel (j), the absolute vertical dust flux in iDust is significantly greater than in CAMS, especially during the long-range dust transport key period. The spatial distribution also highlights that iDust exhibits much stronger vertical dust flux than CAMS. Overall, iDust demonstrates stronger long-range transport, along with enhanced vertical dust activity, possibly due to its high-resolution dynamics. In contrast, both models exhibit largely consistent characteristics with horizontal dynamics. The model analysis is performed at 700 hPa (except for DOD), and the same conclusion can also be drawn from the horizontal and vertical kinetic energy at other pressure levels, as shown in Figures S7 and S8 of Supporting Information S1.

To investigate how much small-scales a model can resolve, the spectral analysis, based on the spherical harmonic decomposition of satellite-observed AOD, DOD, and model-simulated DOD on March 15th is presented in Figure 11, with gray dashed-dotted line representing a reference line of -3 power law. All data used for the spectral analysis are global, with missing values in satellite observations filled with zero. The observations, both AOD and DOD, show greater DOD variance than GCM products. Possible reasons for this difference may include overestimation of AOD satellite observations (Gupta et al., 2018; Li et al., 2020), and the fact that satellite observations are conducted during the daytime when dust activity is more pronounced. Despite these limitations, the observations remain a valuable reference for gauging the relative DOD intensities across different scales. For characteristic spatial scales finer than 100 km, CAMS and MERRA2's resolving ability diminishes rapidly. In

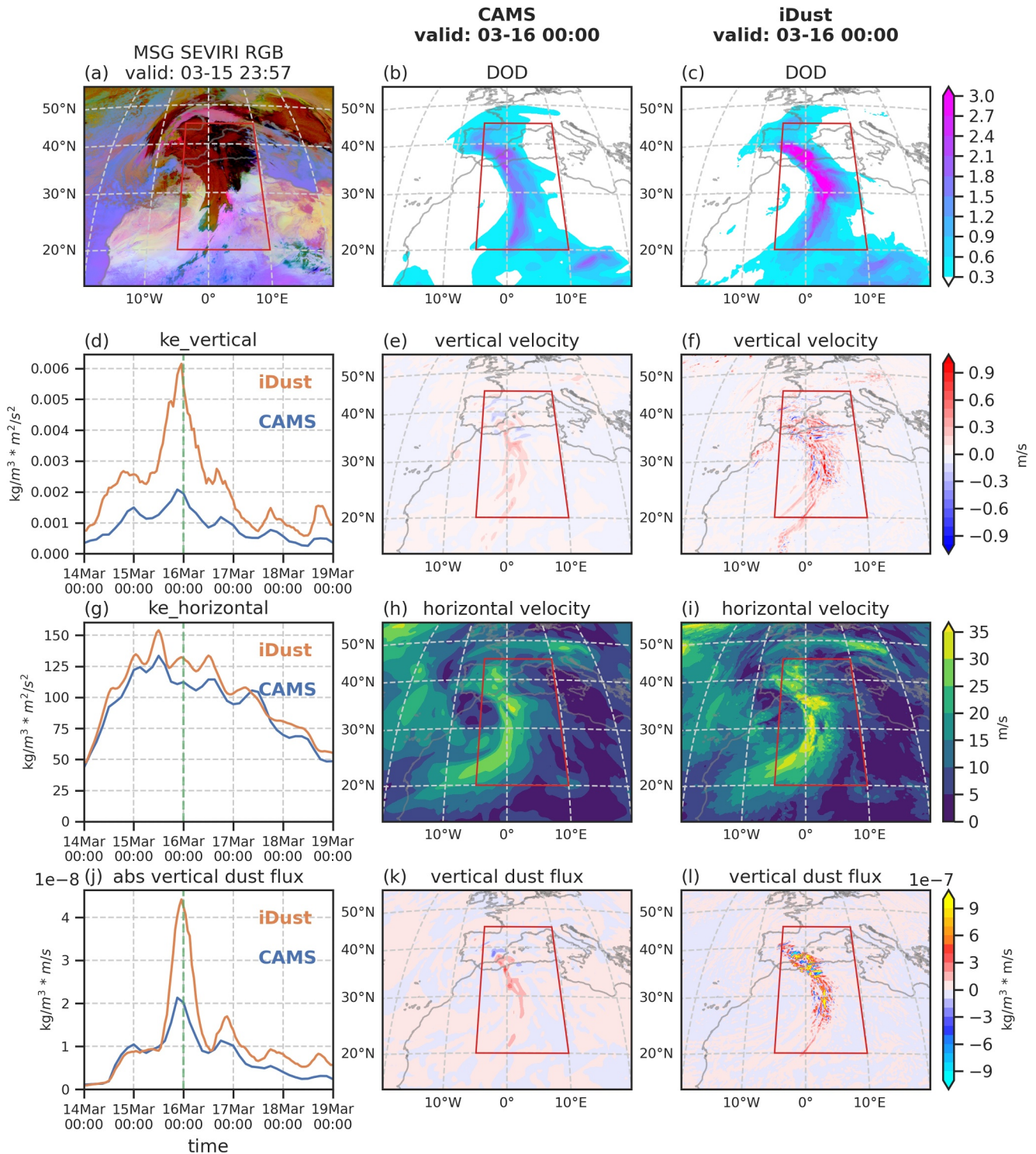


Figure 10. (a) SEVIRI-observed dust RGB image and comparison between (b) CAM5 and (c) iDust DOD. (e and f) The vertical velocity, (h and i) horizontal velocity, and (k and l) the vertical dust flux in 700 hPa. Panels (d), (g), and (j) show time series of vertical kinetic energy, horizontal kinetic energy, and vertical dust activity from 14 to 18 March 2022, respectively. All spatial distributions are at 00:00 on 16 March 2022, as marked by the green lines in panels (d), (g), and (j). Time series panels represent mean values for the area within the red box in the spatial distribution maps, calculated after remapping to a 0.4-degree resolution. Both CAM5 and iDust were initiated at 00:00 on 14 March 2022.

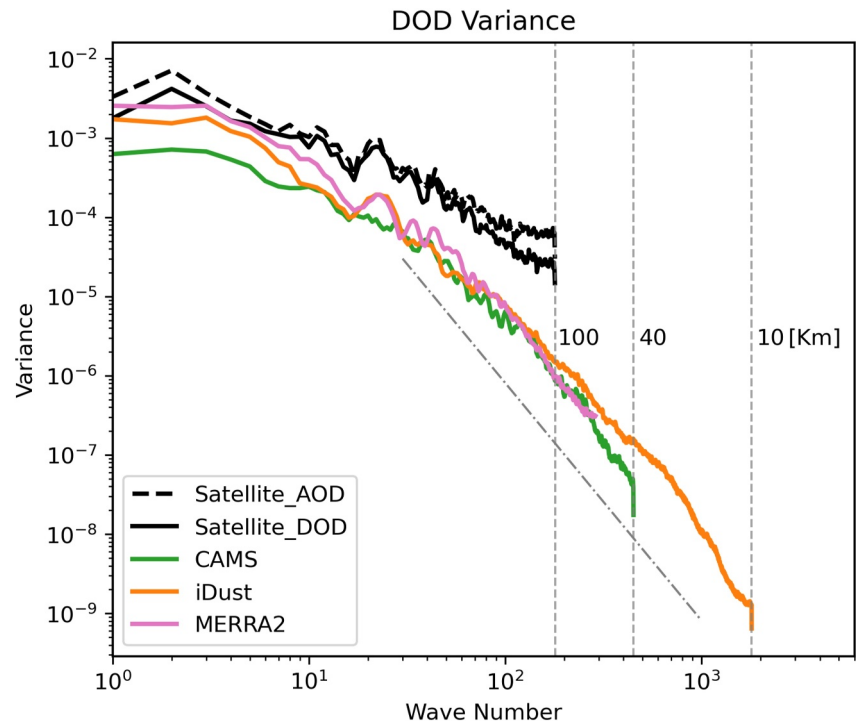


Figure 11. Spectral analysis of the satellite observed DOD (solid black line) and AOD (dashed black line) on March 15th, along with the simulated DOD by CAMS (green line), iDust (orange line), and MERRA2 (pink line) at 12:00 UTC on March 15th. The gray dash-dotted line represents a reference -3 power law.

contrast, iDust, with its higher spatial resolution, demonstrates encouraging capability in resolving small-scale features that are crucial for accurately representing extreme processes.

4.3. The 2020 “Godzilla” Saharan Dust Plume

In June 2020, a colossal dust plume dubbed “Godzilla” journeyed from the Sahara Desert across the Atlantic Ocean to the Caribbean Sea (Pu & Jin, 2021). Satellite observations, reanalysis data, and models depict the spatial distribution of DOD for this event, as shown in Figure 12. While CAMS and iDust project slightly weaker DOD intensities, the overall spatial distribution appears reasonable. Based on the RMSE and correlation coefficient, MERRA2 demonstrates the best performance, while iDust shows a similar RMSE but a significantly higher correlation coefficient compared to CAMS. It is important to note that iDust forecasts, initialized with MERRA2 dust fields, have intensities highly dependent on MERRA2 characteristics, especially toward the later periods, highlighting the need for accurate initialization data in forecasting models. Despite this dependency, all models provide excellent spatial patterns of the DOD for this significant event, demonstrating their capabilities in tracking and analyzing dust transport phenomena.

The CALIPSO observations and cross-section of model results along the CALIPSO trajectory (see orange lines in Figure 12), are illustrated in Figure 13. All three models demonstrate reasonable reproduction of the dust vertical distribution during this event, with iDust offering the most finely detailed representation. On the 13th, while MERRA2 reanalysis and CAMS closely align with the observations, only iDust accurately simulates the vertical lifting of dust at 25°N . On the 15th, the three numerical models adequately describe dust transport's vertical and meridional distribution despite incomplete satellite observations at lower levels. iDust effectively simulates the vertical lifting of intense dust emission over land on the 17th, as depicted in Figure 12's third row. Furthermore, iDust finely depicts the high-frequency wave train at the base of the dust cloud during its propagation on the 21st and 23rd, attributed to its high resolution and non-hydrostatic features (X. Chen et al., 2013). The results indicate that iDust can capture detailed vertical distribution and small-scale dynamic features of dust transport events.

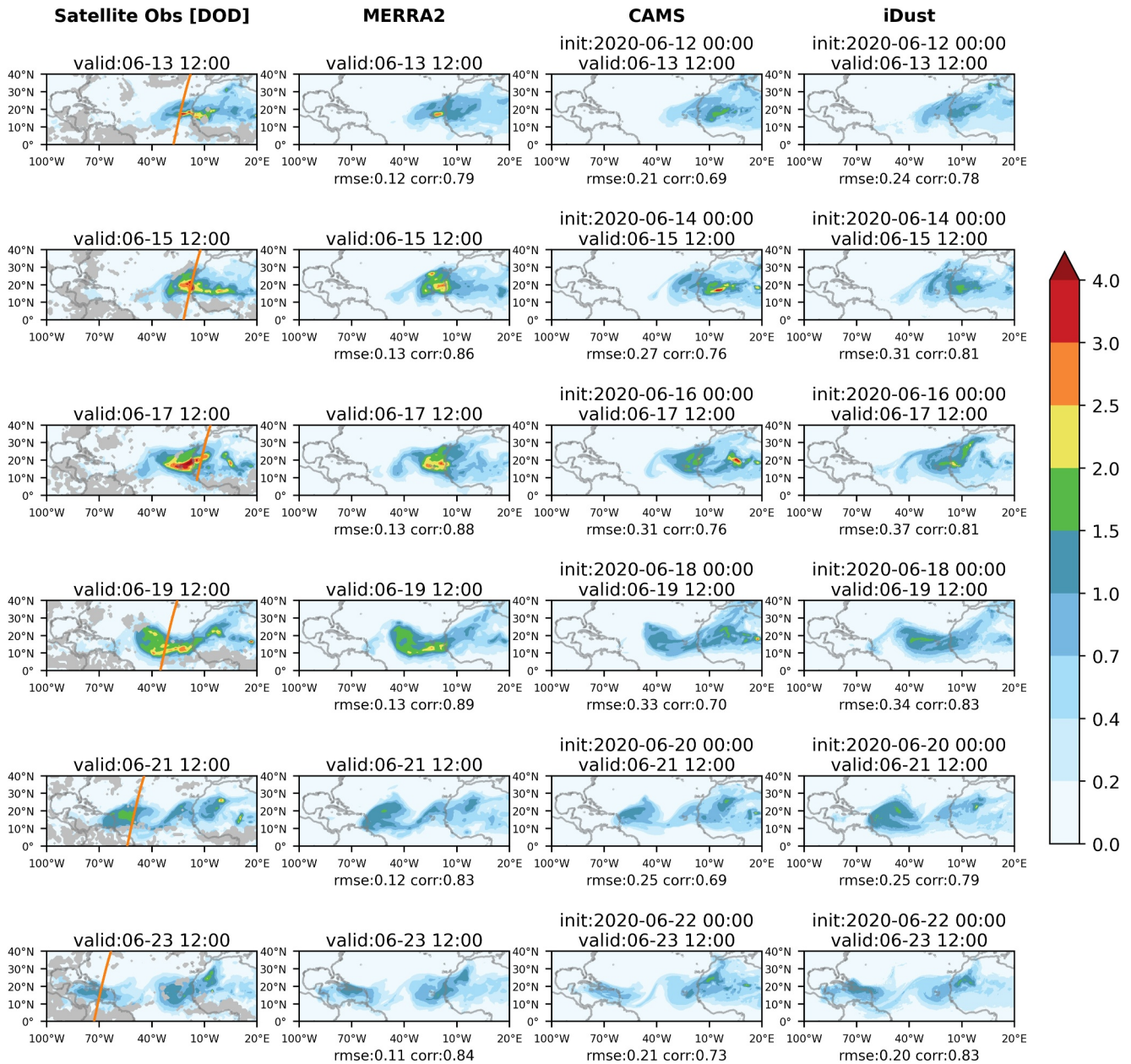


Figure 12. The spatial distribution of satellite-observed DOD (first column), and DOD simulated by MERRA2 reanalysis (second column), CAMS (third column), and iDust (fourth column) during the Godzilla dust event (13–23 June 2020). RMSE and correlation coefficient are shown below each panel. The orange line in the first column represents the trajectory of CALIPSO used in Figure 13.

Five AERONET sites (Figure 14a) along the dust propagation path, providing 500 nm AOD observations, are selected to validate model simulation results with better temporal coverage. Figures 14b–14f show the time series of AOD observations and DOD from models at these sites. Dakar Belair and Capo Verde reflect dust initiation and short-range propagation from North Africa, while the other three sites reflect long-range propagation. MERRA2 reanalysis consistency with AERONET observations implies desirable assimilation. CAMS and iDust reproduced DOD change trends at Dakar Belair and Capo Verde, albeit weaker than observations. iDust initialized on March 10th and 12th both well simulate the dust affecting the Caribbean around March 21st, highlighting its 5-to-10-day forecast accuracy. In contrast, CAMS only provides forecasts for the next 5 days. The three Caribbean sites experienced significant AOD increases due to dust from March 21st to 25th, which can be captured by CAMS and iDust. However, iDust's DOD intensity is closer to observations. The results indicate that iDust effectively

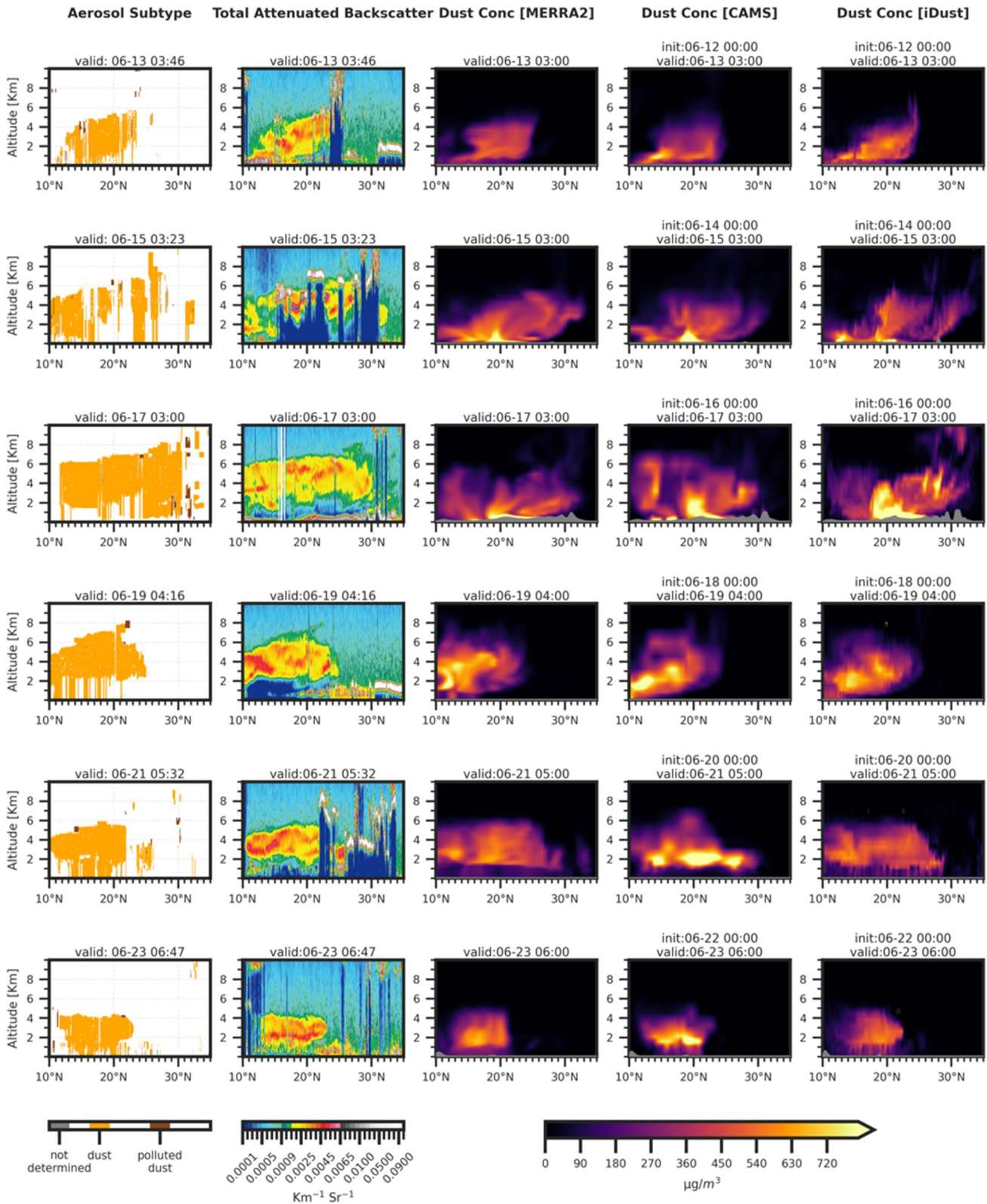


Figure 13. CALIPSO observed Vertical Feature Mask (VFM, first column), total attenuated backscatter at 532 nm (unit: $\text{km}^{-1} \text{Sr}^{-1}$; second column), and dust concentration simulated by MERRA2, CAMS, and iDust (unit: $\mu\text{g}/\text{m}^3$; third to fifth columns) along the CALIPSO trajectory (orange lines in Figure 12) during the “Godzilla” dust event.

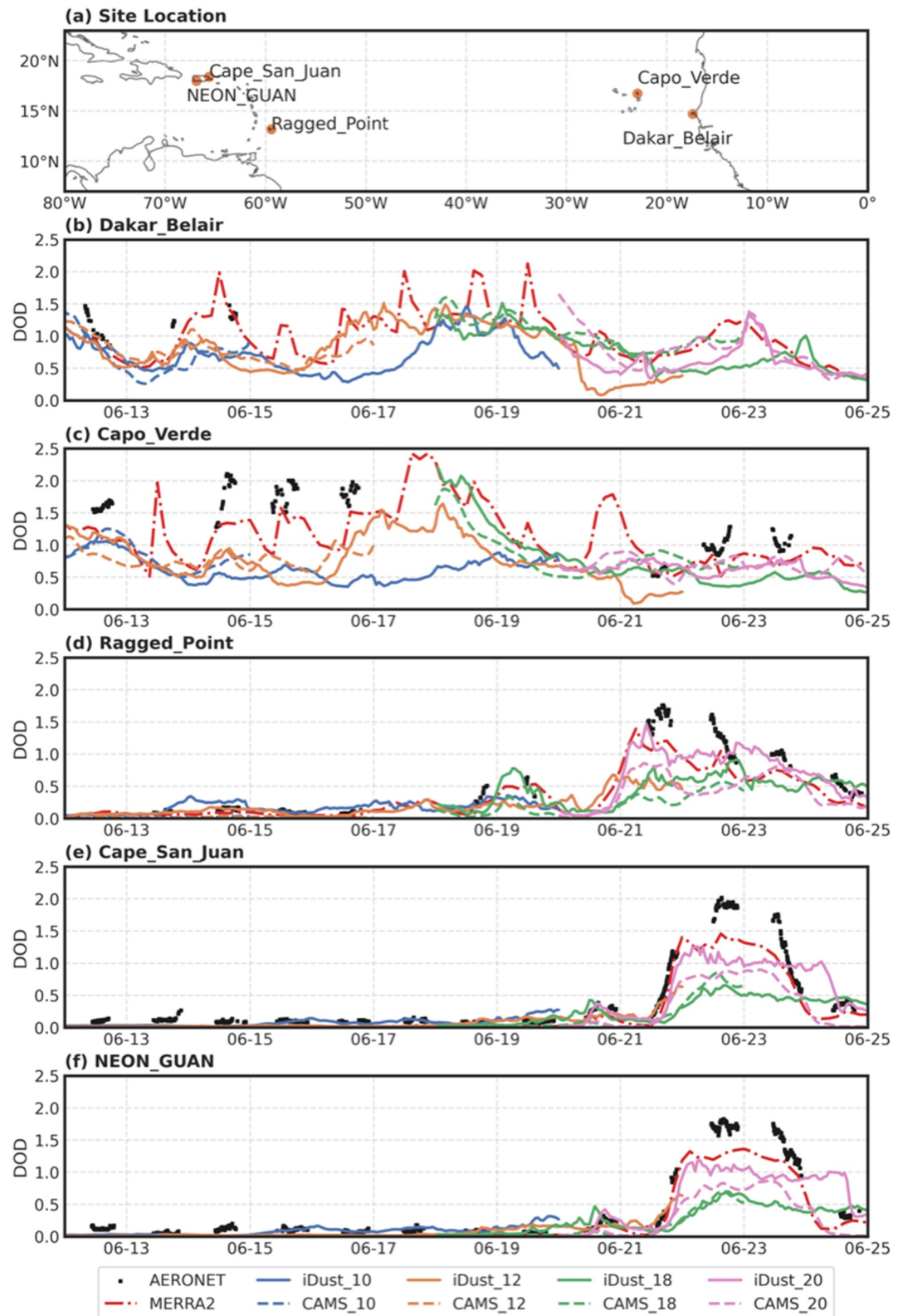


Figure 14. (a) The location of five selected AERONET sites with level 2 observation of 500 nm AOD available, and (b–f) the time series of AOD observations and DOD from MERRA2, CAMS, and iDust at these five sites. The number after the underscore denotes the initial day of model forecasts.

simulates this long-range transport dust event, demonstrating the capability to forecast the impact of dust events at specific locations up to 10 days in advance.

4.4. Computational Performance and Tuning Suggestions of Dust Emission Algorithms

iDust's ultra-high computational efficiency, achieved through inline dust processes, is crucial for this work. Tests have been conducted to quantify the additional computational power required for the dust-related processes in iDust by toggling dust-related calculations on and off. On an AMD first generation EPYC computing platform with 2,304 threads ($16 \times 24 \times 6$), iDust required 6469 s to complete a 10-day integration calculation, while SHIELD (iDust with dust turned off) took 5,752 s for the matching calculation without dust-related calculations. This test indicates that iDust only needs to increase computational power by approximately 12.5% to support global 12.5 km resolution NWP-Grade real-time dust forecasting capabilities.

In real simulation scenarios, the 10-day iDust forecast, starting from 00:00 UTC, can be completed by 06:00 UTC. As comparison, CAMS, with a 40 km resolution and a 5-day forecast duration, can only be obtained at 10:00 UTC (<https://confluence.ecmwf.int/display/CKB/CAMS/3A+Global+atmospheric+composition+forecast+data+documentation>; last accessed on 2024-06-04). Therefore, by investing an extra 1/8 of NWP computational resources, the iDust NWP-dust integrated paradigm offers the renewable energy industry earlier dust forecasts at a higher resolution, with more extended lead times and better representation of extreme dust storms.

Lastly, focusing on extreme dust storms requires a different model calibration approach than traditional low-resolution aerosol climate models. Climate simulations neglect tuning strong winds, leading to substantial uncaptured dust simulation biases due to infrequent strong wind events. On the other hand, the threshold velocity u_t is traditionally estimated from wind tunnels, and direct usage of observationally derived u_t yields problematic dust emissions when strong winds are significantly underestimated. Adjusting the overall dust rate (e.g., increasing C) to obtain reasonable equilibrium simulations cannot represent local extreme events correctly. Therefore, the following procedures are recommended for the best extreme event simulations:

1. Improve strong wind simulations.
2. Adjust u_t value based on strong wind biases.
3. Fine-tune the rest of relevant parameters.

This approach enhances the ability to simulate extreme dust events in high-resolution weather models by effectively utilizing observational data.

5. Conclusions and Discussions

A full-fledged aerosol forecast model with extensive modules and sophisticated parameterizations may not offer optimal solutions when focusing on specific targets emphasizing intensity and localized features. This study found that models like CAMS and MERRA2, despite their comprehensive aerosol-chemistry packages, exhibited limited capabilities in simulating severe dust storms. Efforts such as variable resolution model configurations, which aim to increase spatial resolution over target areas (Feng et al., 2023; Liang et al., 2021; Yue et al., 2023), have yet to address the substantial computational burden of the chemical aerosol module, resulting in a finest resolution of 16–25 km that still requires improvement for a more precise assessment of dust storm weather impacts.

This study adopts a novel paradigm, prioritizing severe dust storm forecasts for the renewable energy sector while minimizing resource utilization. The iDust model achieves a globally uniform 12.5 km resolution by integrating dust processes into the dynamical core. Employing high spatial resolution in dust emission, transport, and deposition processes and updating them at the highest available frequency, produce simulations that accurately capture dust storm intensity. Furthermore, its high-resolution dynamics offer stronger updrafts than low-resolution dynamics, enhancing vertical dust transport in crucial areas, better aligning with observations, and improving long-range transport prediction skills of dust storms. The Dust-NWP integrated practice also facilitates authentic real-time availability of dust forecast products. The iDust model calculates dust forecasts with only a 12.5% increase in computational resource consumption. This allows the 00:00 UTC iDust 10-day forecast to be available at 06:00 UTC with a resolution of 12.5 km. In contrast, CAMS, which produces only a fewer 5-day forecast with a resolution of 40 km, is typically available at 10:00 UTC. Although it does not encompass the

full range of aerosol effects, iDust fills the gap in high-resolution dust storm simulations, aiming to better forecast small-scale extreme hazardous events.

Severe dust storms can significantly disrupt photovoltaic power generation, leading to surges in electricity prices. iDust mitigates potential losses by predicting the occurrence of these extreme events. This study also reveals that certain regions in northwestern China, previously considered abundant in solar resources, may need to discount up to 25% of their theoretical solar energy potential due to dust deposition on photovoltaic surfaces alone. This discount will likely be more substantial when considering the adverse effects of dust scattering on solar radiation (Evans et al., 2019; Pérez et al., 2006; Rodwell & Jung, 2008), highlighting the need for further investigation.

This work is the initial step toward establishing capabilities to capture extreme dust events in a Numerical Weather Prediction system. Future research will focus on enhancing other iDust components, with one of the highest priorities being accurate initial dust conditions (Lu et al., 2022). A better-balanced iDust mean state with more reasonable initial conditions or a longer integration time, such as with carefully designed nudging techniques, can offer a unique research tool to study the dust budget in the Earth's climate system. Also, this work treats the wind erosion threshold velocity u_t as a constant, but more sophisticated treatments can be employed for different surfaces and wind speed characteristics (Pu et al., 2020). The impact of dust on radiative feedback, affecting surface solar resource prediction, and its potential to act as condensation nuclei, influencing cloud formation (Zeng et al., 2023) warrant further investigation. Finally, significant uncertainty in dust size distribution in current models (Huang et al., 2019; Kok, 2011) impacts dust spatial-temporal distribution and transport, necessitating further research. Ensemble dust forecasting and Machine Learning integration are also attractive directions for future model development.

At the time of the writing, iDust has also been successfully integrated into the fully GPU-powered TianJi Numerical Weather Prediction (NWP) system, enabling real-time dust forecasts quasi-operationally at 00UTC and 12UTC daily (available at: <https://www.tjweather.com/dust>; last accessed on 2024-12-19). Developed by TianJi Weather Science and Technology Company (founded in 2021), TianJi NWP is a unified global-to-regional prediction system delivering high-resolution weather forecasts with exceptional accuracy and efficiency. TianJi's impressive computational performance opens up exciting opportunities for dust forecast applications, such as running variable-resolution settings to focus on extended regions at a high horizontal resolution of 2.5 km while maintaining global coverage, particularly intriguing for simulating or forecasting extremely small-scale Haboob events (Bukowski & van den Heever, 2021; Gu et al., 2021). Furthermore, TianJi's ability to run a 12.5 km configuration for extended periods at relatively low computational costs enables high-resolution dust forecasting applications on seasonal-to-sub-seasonal scales, as explored by Yu et al. (2015) and Pu et al. (2019), providing valuable insights into dust transport patterns, air quality, and their impacts on climate and human health.

iDust's development and successful implementation marks a significant advancement in dust forecasting, delivering accurate, efficient, and high-resolution dust predictions in real-time across various temporal and spatial scales. By integrating dust processes directly into the model's dynamical core, iDust provides a more realistic representation of dust emission, transport, and deposition while minimizing computational costs. As the world transitions towards renewable energy, accurate and timely dust forecasts will be crucial for optimizing the design, maintenance, and operation of solar and wind energy infrastructure in dust-prone regions. iDust paves the way for a new era of dust forecasting, providing valuable insights and decision support for the renewable energy industry, policymakers, and the public. With further advancements in dust data assimilation, parameterization, and dust-radiation-cloud interactions, iDust can revolutionize our understanding and management of dust events, contributing to a more sustainable and resilient future.

Data Availability Statement

Hourly 10-m Wind observations are obtained from the China Meteorological Data Service Centre (CMDC, 2023). PM10 observations are obtained from China's National Environmental Monitoring Center (CNEMC, 2023) and the Ministry for Ecological Transition and Demographic Challenge in Spain (MITECO, 2022). The AD-Net Data set is obtained from the Asian dust and aerosol lidar observation network (AD-Net, 2023). The short-wave radiation downward observation for station Tamanrasset is provided by Baika and Saanoune (2022). The AERONET AOD is obtained from AERONET (2020). AOD from MODIS (Platnick et al., 2017a, 2017b) and VIIRS (VIIRS Atmosphere Science Team, 2023a, 2023b) can be downloaded from Level-1 and Atmosphere Archive &

Distribution System Distributed Active Archive Center. The data set for dust RGB images is hosted at EUMETSAT (2022). The CALIPSO observations (NASA/LARC/SD/ASDC, 2023a, 2023b) are obtained from the NASA Langley Research Center Atmospheric Science Data Center. MERRA2 (Global Modeling and Assimilation Office, 2015a, 2015b, 2015c) is obtained from the Goddard Earth Sciences Data and Information Services Center (GES DISC). CAMS forecast data is obtained from ECMWF (2023). ERA5 is obtained from Copernicus Climate Change Service (C3S) (2023). The Source code of iDust is hosted at X. Chen et al. (2024). The FV3/SHiELD source code is hosted at https://github.com/NOAA-GFDL/GFDL_atmos_cubed_sphere and https://github.com/NOAA-GFDL/SHiELD_physics. TianJi NWP is a commercial product from TianJi Weather Science and Technology Company and can be further consulted at <https://www.tjweather.com>.

Acknowledgments

GFDL, particularly Lucas Harris and Linjong Zhou, provided vast support from the SHiELD team. The authors want to thank John Dunne for the constructive GFDL internal review. The authors sincerely appreciate the valuable feedback from editor Jiwen Fan, the anonymous associated editor, and three anonymous reviewers, which greatly improved the quality of this paper. This research has been supported by the National Natural Science Foundation of China (42288101, 42275174), Chinese Academy of Science Light of the West Interdisciplinary Research Grant (Grant xbzgzdsys-202104), and award NA18OAR4320123 from the National Oceanic and Atmospheric Administration, U.S. Department of Commerce. The authors also thank SuperComputing Network (SCNet) for its support during the development.

References

- AD-Net. (2023). The Asian dust and aerosol lidar observation network [Dataset]. Retrieved from <https://www-lidar.nies.go.jp/AD-Net/ncdf/SNS/AERONET>.
- AERONET. (2020). AERONET AOD [Dataset]. Retrieved from https://aeronet.gsfc.nasa.gov/new_web/webtool_aod_v3.html
- Agustí-Panareda, A., Diamantakis, M., Massart, S., Chevallier, F., Muñoz-Sabater, J., Barré, J., et al. (2019). Modelling CO₂ weather—Why horizontal resolution matters. *Atmospheric Chemistry and Physics*, 19(11), 7347–7376. <https://doi.org/10.5194/acp-19-7347-2019>
- Alpert, J. C. (2004). Sub-grid scale mountain blocking at NCEP. In *Proceedings of 20th Conference on WAF, 16th Conference on NWP*. Citeseer.
- Antón, M., Valenzuela, A., Román, R., Lyamani, H., Krotkov, N., Arola, A., et al. (2012). Influence of desert dust intrusions on ground-based and satellite-derived ultraviolet irradiance in southeastern Spain. *Journal of Geophysical Research*, 117(D19), 2012JD018056. <https://doi.org/10.1029/2012JD018056>
- Baika, S., & Saanouné, A. (2022). Basic measurements of radiation at station Tamanrasset (2022-03) [Dataset]. PANGAEA. <https://doi.org/10.1594/PANGAEA.943383>
- Balkanski, Y., Schulz, M., Claquin, T., & Guibert, S. (2007). Reevaluation of Mineral aerosol radiative forcings suggests a better agreement with satellite and AERONET data. *Atmospheric Chemistry and Physics*, 7(1), 81–95. <https://doi.org/10.5194/acp-7-81-2007>
- Banks, J., & Brindley, H. (2013). Evaluation of MSG-SEVIRI mineral dust retrieval products over North Africa and the Middle East. *Remote Sensing of Environment*, 128, 58–73. <https://doi.org/10.1016/j.rse.2012.07.017>
- Basart, S., Pérez, C., Nickovic, S., Cuevas, E., & Baldasano, J. (2012). Development and evaluation of the BSC-DREAM8b dust regional model over Northern Africa, the Mediterranean and the Middle East. *Tellus B: Chemical and Physical Meteorology*, 64(1), 18539. <https://doi.org/10.3402/tellusb.v64i0.18539>
- Benedetti, A., Morcrette, J.-J., Boucher, O., Dethof, A., Engelen, R. J., Fisher, M., et al. (2009). Aerosol analysis and forecast in the European Centre for Medium-Range Weather Forecasts Integrated Forecast System: 2. Data assimilation. *Journal of Geophysical Research*, 114(D13). <https://doi.org/10.1029/2008JD011115>
- Bhattacharjee, P. S., Wang, J., Lu, C.-H., & Tallapragada, V. (2018). The implementation of NEMS GFS Aerosol Component (NGAC) Version 2.0 for global multispecies forecasting at NOAA/NCEP—Part 2: Evaluation of aerosol optical thickness. *Geoscientific Model Development*, 11(6), 2333–2351. <https://doi.org/10.5194/gmd-11-2333-2018>
- Bosilovich, M. G., Lucchesi, R., & Suarez, M. (2016). MERRA-2: File specification. GMAO Office Note No. 9 (Version 1.1) (Tech. Rep.). Goddard Space Flight Center: GMAO, NASA GSFC.
- Buchard, V., Randles, C. A., da Silva, A. M., Darmenov, A., Colarco, P. R., Govindaraju, R., et al. (2017). The MERRA-2 aerosol reanalysis, 1980 onward. Part II: Evaluation and case studies. *Journal of Climate*, 30(17), 6851–6872. <https://doi.org/10.1175/JCLI-D-16-0613.1>
- Bukowski, J., & van den Heever, S. C. (2021). Direct radiative effects in Haboobs. *Journal of Geophysical Research: Atmospheres*, 126(21). <https://doi.org/10.1029/2021JD034814>
- Chakraborty, S., Guan, B., Waliser, D. E., & Da Silva, A. M. (2022). Aerosol atmospheric rivers: Climatology, event characteristics, and detection algorithm sensitivities. *Atmospheric Chemistry and Physics*, 22(12), 8175–8195. <https://doi.org/10.5194/acp-22-8175-2022>
- Chen, S., Zhao, D., Huang, J., He, J., Chen, Y., Chen, J., et al. (2023). Mongolia contributed more than 42% of the dust concentrations in Northern China in March and April 2023. *Advances in Atmospheric Sciences*, 40(9), 1549–1557. <https://doi.org/10.1007/s00376-023-3062-1>
- Chen, X., Andronova, N., Van Leer, B., Penner, J. E., Boyd, J. P., Jablonowski, C., & Lin, S.-J. (2013). A control-volume model of the compressible Euler equations with a vertical Lagrangian coordinate. *Monthly Weather Review*, 141(7), 2526–2544. <https://doi.org/10.1175/MWR-D-12-00129.1>
- Chen, X., Chong, M., Lin, S.-J., Liang, Z., Ginoux, P., Liang, Y., et al. (2024). iDust source code [Software]. Zenodo. <https://doi.org/10.5281/zenodo.11364306>
- Chen, X., Lin, G., & Fu, Z. (2007). Long-range correlations in daily relative humidity fluctuations: A new index to characterize the climate regions over China. *Geophysical Research Letters*, 34(7). <https://doi.org/10.1029/2006gl027755>
- Chen, X., Lin, S.-J., & Harris, L. M. (2018). Towards an unstaggered finite-volume dynamical core with a fast Riemann solver: 1-D linearized analysis of dissipation, dispersion, and noise control. *Journal of Advances in Modeling Earth Systems*, 10(9), 2333–2356. <https://doi.org/10.1029/2018ms001361>
- Chin, M., Ginoux, P., Kinne, S., Torres, O., Holben, B. N., Duncan, B. N., et al. (2002). Tropospheric aerosol optical thickness from the GOCART model and comparisons with satellite and sun photometer measurements. *Journal of the Atmospheric Sciences*, 59(3), 461–483. [https://doi.org/10.1175/1520-0469\(2002\)059<0461:TAOTFT>2.0.CO;2](https://doi.org/10.1175/1520-0469(2002)059<0461:TAOTFT>2.0.CO;2)
- Chin, M., Rood, R. B., Lin, S.-J., Müller, J.-F., & Thompson, A. M. (2000). Atmospheric sulfur cycle simulated in the global model GOCART: Model description and global properties. *Journal of Geophysical Research*, 105(D20), 24671–24687. <https://doi.org/10.1029/2000JD900384>
- Chun, H.-Y., & Baik, J.-J. (1998). Momentum flux by thermally induced internal gravity waves and its approximation for large-scale models. *Journal of the Atmospheric Sciences*, 55(21), 3299–3310. [https://doi.org/10.1175/1520-0469\(1998\)055<3299:MFBTHI>2.0.CO;2](https://doi.org/10.1175/1520-0469(1998)055<3299:MFBTHI>2.0.CO;2)
- Clough, S., Shephard, M., Mlawer, E., Delamere, J., Iacono, M., Cady-Pereira, K., et al. (2005). Atmospheric radiative transfer modeling: A summary of the AER codes. *Journal of Quantitative Spectroscopy and Radiative Transfer*, 91(2), 233–244. <https://doi.org/10.1016/j.jqsrt.2004.05.058>
- CMDC. (2023). Daily timed data from automated weather stations in China [Dataset]. Retrieved from <https://data.cma.cn/en/?r=data/detail&dataCode=A.0012.0001>
- CNEMC. (2023). PM10 [Dataset]. Retrieved from <https://air.cnemc.cn:18007/>

- Colarco, P., da Silva, A., Chin, M., & Diehl, T. (2010). Online simulations of global aerosol distributions in the NASA GEOS-4 model and comparisons to satellite and ground-based aerosol optical depth. *Journal of Geophysical Research*, *115*(D14), D14207. <https://doi.org/10.1029/2009JD012820>
- Colarco, P. R., Nowottnick, E. P., Randles, C. A., Yi, B., Yang, P., Kim, K.-M., et al. (2014). Impact of radiatively interactive dust aerosols in the NASA GEOS-5 climate model: Sensitivity to dust particle shape and refractive index. *Journal of Geophysical Research: Atmospheres*, *119*(2), 753–786. <https://doi.org/10.1002/2013JD020046>
- Collow, A., Buchard, V. J., Chin, M., Colarco, P. R., Darmanov, A. S., & Da Silva, A. M. (2022). *Supplemental documentation for GEOS aerosol products* (Tech. Rep.). Goddard Space Flight Center: GMAO, NASA GSFC.
- Copernicus Climate Change Service (C3S). (2023). ERA5 hourly data on single levels from 1940 to present. *Copernicus Climate Change Service (C3S) Climate Data Store (CDS)*. <https://doi.org/10.24381/CDS.ADBB2D47>
- Danabasoglu, G., Lamarque, J.-F., Bacmeister, J., Bailey, D. A., DuVivier, A. K., Edwards, J., et al. (2020). The Community Earth System Model Version 2 (CESM2). *Journal of Advances in Modeling Earth Systems*, *12*(2), e2019MS001916. <https://doi.org/10.1029/2019MS001916>
- De Boyer Montégut, C., Madec, G., Fischer, A. S., Lazar, A., & Iudicone, D. (2004). Mixed layer depth over the global ocean: An examination of profile data and a profile-based climatology. *Journal of Geophysical Research*, *109*(C12), 2004JC002378. <https://doi.org/10.1029/2004JC002378>
- Driemel, A., Augustine, J., Behrens, K., Colle, S., Cox, C., Cuevas-Agulló, E., et al. (2018). Baseline surface radiation network (BSRN): Structure and data description (1992–2017). *Earth System Science Data*, *10*(3), 1491–1501. <https://doi.org/10.5194/essd-10-1491-2018>
- ECMWF. (2023). CAMS global atmospheric composition forecasts [Dataset]. Retrieved from <https://ads.atmosphere.copernicus.eu/datasets/cams-global-atmospheric-composition-forecasts?tab=download>
- Ek, M. B., Mitchell, K. E., Lin, Y., Rogers, E., Grunmann, P., Koren, V., et al. (2003). Implementation of Noah land surface model advances in the National Centers for Environmental Prediction operational mesoscale Eta model. *Journal of Geophysical Research*, *108*(D22), 2002JD003296. <https://doi.org/10.1029/2002JD003296>
- Eskes, H., Huijnen, V., Arola, A., Benedictow, A., Blechschmidt, A.-M., Botek, E., et al. (2015). Validation of reactive gases and aerosols in the MACC global analysis and forecast system. *Geoscientific Model Development*, *8*(11), 3523–3543. <https://doi.org/10.5194/gmd-8-3523-2015>
- EUMETSAT. (2022). High Rate SEVIRI Level 1.5 Image Data—MSG—0 degree [Dataset]. Retrieved from <https://data.eumetsat.int/data/map/EO:EUM:DAT:MSG:HRSEVIRI>
- Evans, S., Malyshev, S., Ginoux, P., & Shevliakova, E. (2019). The impacts of the dust radiative effect on vegetation growth in the Sahel. *Global Biogeochemical Cycles*, *33*(12), 1582–1593. <https://doi.org/10.1029/2018GB006128>
- Feng, J., Zhao, C., Du, Q., Xu, M., Gu, J., Hu, Z., & Chen, Y. (2023). Simulating atmospheric dust with a global variable-resolution model: Model description and impacts of Mesh Refinement. *Journal of Advances in Modeling Earth Systems*, *15*(10), e2023MS003636. <https://doi.org/10.1029/2023MS003636>
- Gallagher, M. W., Nemitz, E., Dorsey, J. R., Fowler, D., Sutton, M. A., Flynn, M., & Duyzer, J. (2002). Measurements and parameterizations of small aerosol deposition velocities to grassland, arable crops, and forest: Influence of surface roughness length on deposition. *Journal of Geophysical Research*, *107*(D12), 4154. <https://doi.org/10.1029/2001JD000817>
- Gelaro, R., McCarty, W., Suárez, M. J., Todling, R., Molod, A., Takacs, L., et al. (2017). The modern-era retrospective analysis for research and applications, Version 2 (MERRA-2). *Journal of Climate*, *30*(14), 5419–5454. <https://doi.org/10.1175/JCLI-D-16-0758.1>
- Gent, P. R., Danabasoglu, G., Donner, L. J., Holland, M. M., Hunke, E. C., Jayne, S. R., et al. (2011). The community climate system model version 4. *Journal of Climate*, *24*(19), 4973–4991. <https://doi.org/10.1175/2011JCLI4083.1>
- Gillette, D. A., & Passi, R. (1988). Modeling dust emission caused by wind erosion. *Journal of Geophysical Research*, *93*(D11), 14233–14242. <https://doi.org/10.1029/JD093iD11p14233>
- Ginoux, P., Chin, M., Tegen, I., Prospero, J. M., Holben, B., Dubovik, O., & Lin, S.-J. (2001). Sources and distributions of dust aerosols simulated with the GOCART model. *Journal of Geophysical Research*, *106*(D17), 20255–20273. <https://doi.org/10.1029/2000JD000053>
- Ginoux, P., Clarisse, L., Clerbaux, C., Coheur, P.-F., Dubovik, O., Hsu, N. C., & Van Damme, M. (2012). Mixing of dust and NH₃ observed globally over anthropogenic dust sources. *Atmospheric Chemistry and Physics*, *12*(16), 7351–7363. <https://doi.org/10.5194/acp-12-7351-2012>
- Ginoux, P., Garbuzov, D., & Hsu, N. C. (2010). Identification of anthropogenic and natural dust sources using Moderate Resolution Imaging Spectroradiometer (MODIS) Deep Blue level 2 data. *Journal of Geophysical Research*, *115*(D5), D05204. <https://doi.org/10.1029/2009JD012398>
- Ginoux, P., Prospero, J. M., Gill, T. E., Hsu, N. C., & Zhao, M. (2012). Global-scale attribution of anthropogenic and natural dust sources and their emission rates based on MODIS Deep Blue aerosol products. *Reviews of Geophysics*, *50*(3). <https://doi.org/10.1029/2012RG000388>
- Global Modeling and Assimilation Office. (2015a). MERRA-2 inst1_2d_asm_Nx: 2d,3-Hourly,Instantaneous,Single-Level,Assimilation,Single-Level Diagnostics V5.12.4 [Dataset]. *NASA Goddard Earth Sciences Data and Information Services Center*. <https://doi.org/10.5067/3Z173KIE2TPD>
- Global Modeling and Assimilation Office. (2015b). MERRA-2 inst3_3d_aer_Nv: 3d,3-Hourly,Instantaneous,Model-Level,Assimilation,Aerosol Mixing Ratio V5.12.4 [Dataset]. *NASA Goddard Earth Sciences Data and Information Services Center*. <https://doi.org/10.5067/LTVB4GPCOTK2>
- Global Modeling and Assimilation Office. (2015c). MERRA-2 inst3_3d_asm_Nv: 3d,3-Hourly,Instantaneous,Model-Level,Assimilation, Assimilated Meteorological Fields V5.12.4 [Dataset]. *NASA Goddard Earth Sciences Data and Information Services Center*. <https://doi.org/10.5067/WWQSQX8IVFW8>
- Greed, G., Haywood, J. M., Milton, S., Keil, A., Christopher, S., Gupta, P., & Highwood, E. J. (2008). Aerosol optical depths over North Africa: 2. Modeling and model validation. *Journal of Geophysical Research*, *113*(D23), D00C05. <https://doi.org/10.1029/2007JD009457>
- Gu, Z., He, Y., Zhang, Y., Su, J., Zhang, R., Yu, C. W., & Zhang, D. (2021). An overview of triggering mechanisms and characteristics of local strong sandstorms in China and Haboobs. *Atmosphere*, *12*(6), 752. <https://doi.org/10.3390/atmos12060752>
- Gupta, P., Remer, L. A., Levy, R. C., & Mattoo, S. (2018). Validation of MODIS 3 km land aerosol optical depth from NASA's EOS Terra and Aqua missions. *Atmospheric Measurement Techniques*, *11*(5), 3145–3159. <https://doi.org/10.5194/amt-11-3145-2018>
- Han, J., & Pan, H.-L. (2011). Revision of convection and vertical diffusion schemes in the NCEP global forecast system. *Weather and Forecasting*, *26*(4), 520–533. <https://doi.org/10.1175/WAF-D-10-05038.1>
- Han, J., Wang, W., Kwon, Y. C., Hong, S.-Y., Tallapragada, V., & Yang, F. (2017). Updates in the NCEP GFS cumulus convection schemes with scale and aerosol awareness. *Weather and Forecasting*, *32*(5), 2005–2017. <https://doi.org/10.1175/WAF-D-17-0046.1>
- Han, J., Witek, M. L., Teixeira, J., Sun, R., Pan, H.-L., Fletcher, J. K., & Bretherton, C. S. (2016). Implementation in the NCEP GFS of a Hybrid Eddy-Diffusivity mass-flux (EDMF) boundary layer parameterization with dissipative heating and modified stable boundary layer mixing. *Weather and Forecasting*, *31*(1), 341–352. <https://doi.org/10.1175/WAF-D-15-0053.1>

- Harris, L., Zhou, L., Lin, S.-J., Chen, J.-H., Chen, X., Gao, K., et al. (2020). GFDL SHIELD: A unified system for weather-to-seasonal prediction. *Journal of Advances in Modeling Earth Systems*, 12(10). <https://doi.org/10.1029/2020MS002223>
- Harris, L. M., & Lin, S.-J. (2014). Global-to-regional nested grid climate simulations in the GFDL high resolution atmospheric model. *Journal of Climate*, 27(13), 4890–4910. <https://doi.org/10.1175/JCLI-D-13-00596.1>
- Haywood, J. M., Allan, R. P., Culverwell, I., Slingo, T., Milton, S., Edwards, J., & Clerbaux, N. (2005). Can desert dust explain the outgoing longwave radiation anomaly over the Sahara during July 2003? *Journal of Geophysical Research*, 110(D5), D05105. <https://doi.org/10.1029/2004JD005232>
- Hersbach, H., Bell, B., Berrisford, P., Hirahara, S., Horányi, A., Muñoz-Sabater, J., et al. (2020). The ERA5 global reanalysis. *Quarterly Journal of the Royal Meteorological Society*, 146(730), 1999–2049. <https://doi.org/10.1002/qj.3803>
- Holben, B., Eck, T., Slutsker, I., Tanré, D., Buis, J., Setzer, A., et al. (1998). AERONET—A federated instrument network and data archive for aerosol characterization. *Remote Sensing of Environment*, 66(1), 1–16. [https://doi.org/10.1016/S0034-4257\(98\)00031-5](https://doi.org/10.1016/S0034-4257(98)00031-5)
- Holben, B., Tanré, D., Smirnov, A., Eck, T. F., Slutsker, I., Abuhassan, N., et al. (2001). An emerging ground-based aerosol climatology: Aerosol optical depth from AERONET. *Journal of Geophysical Research*, 106(D11), 12067–12097. <https://doi.org/10.1029/2001jd900014>
- Hollingsworth, A., Engelen, R. J., Textor, C., Benedetti, A., Boucher, O., Chevallier, F., et al. (2008). Toward a monitoring and forecasting system for atmospheric composition: The GEMS project. *Bulletin of the American Meteorological Society*, 89(8), 1147–1164. <https://doi.org/10.1175/2008BAMS2355.1>
- Hong, S.-Y. (2010). A new stable boundary-layer mixing scheme and its impact on the simulated East Asian summer monsoon. *Quarterly Journal of the Royal Meteorological Society*, 136(651), 1481–1496. <https://doi.org/10.1002/qj.665>
- Horowitz, L. W., Naik, V., Paulot, F., Ginoux, P. A., Dunne, J. P., Mao, J., et al. (2020). The GFDL global atmospheric chemistry-climate model AM4.1: Model description and simulation characteristics. *Journal of Advances in Modeling Earth Systems*, 12(10). <https://doi.org/10.1029/2019MS002032>
- Hsu, N. C., Lee, J., Sayer, A. M., Kim, W., Bettenhausen, C., & Tsay, S.-C. (2019). VIIRS deep blue aerosol products over land: Extending the EOS long-term aerosol data records. *Journal of Geophysical Research: Atmospheres*, 124(7), 4026–4053. <https://doi.org/10.1029/2018JD029688>
- Hu, Z., Zhao, C., Leung, L. R., Du, Q., Ma, Y., Hagos, S., et al. (2022). Characterizing the impact of atmospheric rivers on aerosols in the western U.S. *Geophysical Research Letters*, 49(7), e2021GL096421. <https://doi.org/10.1029/2021GL096421>
- Huang, Y., Kok, J. F., Martin, R. L., Swet, N., Katra, I., Gill, T. E., et al. (2019). Fine dust emissions from active sands at coastal Oceano Dunes, California. *Atmospheric Chemistry and Physics*, 19(5), 2947–2964. <https://doi.org/10.5194/acp-19-2947-2019>
- Huneeus, N., Schulz, M., Balkanski, Y., Griesfeller, J., Prospero, J., Kinne, S., et al. (2011). Global dust model intercomparison in AeroCom phase I. *Atmospheric Chemistry and Physics*, 11(15), 7781–7816. <https://doi.org/10.5194/acp-11-7781-2011>
- Johnson, B. T., Brooks, M. E., Walters, D., Woodward, S., Christopher, S., & Schepanski, K. (2011). Assessment of the Met Office dust forecast model using observations from the GERBILS campaign. *Quarterly Journal of the Royal Meteorological Society*, 137(658), 1131–1148. <https://doi.org/10.1002/qj.736>
- Kok, J. F. (2011). A scaling theory for the size distribution of emitted dust aerosols suggests climate models underestimate the size of the global dust cycle. *Proceedings of the National Academy of Sciences of the United States of America*, 108(3), 1016–1021. <https://doi.org/10.1073/pnas.1014798108>
- Lapere, R., Thomas, J. L., Favier, V., Angot, H., Asplund, J., Ekman, A. M. L., et al. (2024). Polar aerosol atmospheric rivers: Detection, characteristics, and potential applications. *Journal of Geophysical Research: Atmospheres*, 129(2), e2023JD039606. <https://doi.org/10.1029/2023JD039606>
- Li, Y., Shi, G., & Sun, Z. (2020). Evaluation and improvement of MODIS aerosol optical depth products over China. *Atmospheric Environment*, 223, 117251. <https://doi.org/10.1016/j.atmosenv.2019.117251>
- Liang, Y., Yang, B., Wang, M., Tang, J., Sakaguchi, K., Leung, L. R., & Xu, X. (2021). Multiscale simulation of precipitation over East Asia by variable resolution CAM-MPAS. *Journal of Advances in Modeling Earth Systems*, 13(11), e2021MS002656. <https://doi.org/10.1029/2021MS002656>
- Liger, E., Hernández, F., Expósito, F. J., Díaz, J. P., Salazar-Carballo, P. A., Gordo, E., et al. (2024). Transport and deposition of radionuclides from northern Africa to the southern Iberian Peninsula and the Canary Islands during the intense dust intrusions of March 2022. *Chemosphere*, 352, 141303. <https://doi.org/10.1016/j.chemosphere.2024.141303>
- Lin, S.-J. (2004). A “Vertically Lagrangian” finite-volume dynamical core for global models. *Monthly Weather Review*, 132(10), 2293–2307. [https://doi.org/10.1175/1520-0493\(2004\)132<2293:AVLFDC>2.0.CO;2](https://doi.org/10.1175/1520-0493(2004)132<2293:AVLFDC>2.0.CO;2)
- Lin, S.-J., & Rood, R. B. (1996). Multidimensional flux-form semi-Lagrangian transport schemes. *Monthly Weather Review*, 124(9), 2046–2070. [https://doi.org/10.1175/1520-0493\(1996\)124<2046:MFFSLT>2.0.CO;2](https://doi.org/10.1175/1520-0493(1996)124<2046:MFFSLT>2.0.CO;2)
- Liu, Z., Wang, H., Zhang, L., Zhou, Y., Zhang, W., Peng, Y., et al. (2022). Incorporation and improvement of a heterogeneous chemistry mechanism in the atmospheric chemistry model GRAPES_Meso5.1/CUACE and its impacts on secondary inorganic aerosol and PM_{2.5} simulations in Middle-Eastern China. *Science of the Total Environment*, 847, 157530. <https://doi.org/10.1016/j.scitotenv.2022.157530>
- Lu, C.-H., da Silva, A., Wang, J., Moorthi, S., Chin, M., Colarco, P., et al. (2016). The implementation of NEMS GFS Aerosol Component (NGAC) Version 1.0 for global dust forecasting at NOAA/NCEP. *Geoscientific Model Development*, 9(5), 1905–1919. <https://doi.org/10.5194/gmd-9-1905-2016>
- Lu, C.-H., Liu, Q., Wei, S.-W., Johnson, B. T., Dang, C., Stegmann, P. G., et al. (2022). The Aerosol Module in the Community Radiative Transfer Model (v2.2 and v2.3): Accounting for aerosol transmittance effects on the radiance observation operator. *Geoscientific Model Development*, 15(3), 1317–1329. <https://doi.org/10.5194/gmd-15-1317-2022>
- Maghami, M. R., Hizam, H., Gomes, C., Radzi, M. A., Rezadad, M. I., & Hajjighorbani, S. (2016). Power loss due to soiling on solar panel: A review. *Renewable and Sustainable Energy Reviews*, 59, 1307–1316. <https://doi.org/10.1016/j.rser.2016.01.044>
- Mangold, A., De Backer, H., De Paepe, B., Dewitte, S., Chiapello, I., Derimian, Y., et al. (2011). Aerosol analysis and forecast in the European Centre for Medium-Range Weather Forecasts Integrated Forecast System: 3. Evaluation by means of case studies. *Journal of Geophysical Research*, 116(D3), D03302. <https://doi.org/10.1029/2010JD014864>
- Marticorena, B., & Bergametti, G. (1995). Modeling the atmospheric dust cycle: I. Design of a soil-derived dust emission scheme. *Journal of Geophysical Research*, 100(D8), 16415–16430. <https://doi.org/10.1029/95jd00690>
- McCormack, J. P., Eckermann, S. D., Siskind, D. E., & McGee, T. J. (2006). CHEM2D-OPP: A new linearized gas-phase ozone photochemistry parameterization for high-altitude NWP and climate models. *Atmospheric Chemistry and Physics*, 6(12), 4943–4972. <https://doi.org/10.5194/acp-6-4943-2006>
- Micheli, L., Almonacid, F., Bessa, J. G., Fernández-Solas, Á., & Fernández, E. F. (2024). The impact of extreme dust storms on the national photovoltaic energy supply. *Sustainable Energy Technologies and Assessments*, 62, 103607. <https://doi.org/10.1016/j.seta.2024.103607>

- Middleton, N. (2017). Desert dust hazards: A global review. *Aeolian Research*, *24*, 53–63. <https://doi.org/10.1016/j.aeolia.2016.12.001>
- Miller, R. L., Knippertz, P., Pérez García-Pando, C., Perlwitz, J. P., & Tegen, I. (2014). Impact of dust radiative forcing upon climate. In P. Knippertz & J.-B. W. Stuut (Eds.), *Mineral dust* (pp. 327–357). Springer Netherlands. https://doi.org/10.1007/978-94-017-8978-3_13
- Miller, R. L., Perlwitz, J., & Tegen, I. (2004). Feedback upon dust emission by dust radiative forcing through the planetary boundary layer. *Journal of Geophysical Research*, *109*(D24), 2004JD004912. <https://doi.org/10.1029/2004JD004912>
- Miller, R. L., & Tegen, I. (1999). Radiative forcing of a tropical direct circulation by soil dust aerosols. *Journal of the Atmospheric Sciences*, *56*(14), 2403–2433. [https://doi.org/10.1175/1520-0469\(1999\)056<2403:RFOATD>2.0.CO;2](https://doi.org/10.1175/1520-0469(1999)056<2403:RFOATD>2.0.CO;2)
- Miller, R. L., Tegen, I., & Perlwitz, J. (2004). Surface radiative forcing by soil dust aerosols and the hydrologic cycle. *Journal of Geophysical Research*, *109*(D4), 2003JD004085. <https://doi.org/10.1029/2003JD004085>
- MITECO. (2022). PM10 [Dataset]. Retrieved from <https://www.miteco.gob.es/es/calidad-y-evaluacion-ambiental/temas/atmosfera-y-calidad-del-aire/calidad-del-aire/evaluacion-datos/datos/datos-oficiales-2022.html>
- Morcrette, J.-J., Boucher, O., Jones, L., Salmond, D., Bechtold, P., Beljaars, A., et al. (2009). Aerosol analysis and forecast in the European Centre for Medium-Range Weather Forecasts Integrated Forecast System: Forward modeling. *Journal of Geophysical Research*, *114*(D6), D06206. <https://doi.org/10.1029/2008JD011235>
- NASA/LARC/SD/ASDC. (2023a). Calipso lidar level 1b profile data, v4-51 [Dataset]. *NASA Langley Atmospheric Science Data Center DAAC*. https://doi.org/10.5067/CALIPSO/CALIPSO/CAL_LID_L1-Standard-V4-51
- NASA/LARC/SD/ASDC. (2023b). Calipso lidar level 2 vertical feature mask (VFM), v4-51 [Dataset]. *NASA Langley Atmospheric Science Data Center DAAC*. https://doi.org/10.5067/CALIPSO/CALIPSO/CAL_LID_L2_VFM-Standard-V4-51
- Nickovic, S., Kallos, G., Papadopoulos, A., & Kakaliagou, O. (2001). A model for prediction of desert dust cycle in the atmosphere. *Journal of Geophysical Research*, *106*(D16), 18113–18129. <https://doi.org/10.1029/2000JD900794>
- Ortiz, P., & Smolarkiewicz, P. K. (2006). Numerical simulation of sand dune evolution in severe winds. *International Journal for Numerical Methods in Fluids*, *50*(10), 1229–1246. <https://doi.org/10.1002/flid.1138>
- Panat, S., & Varanasi, K. K. (2022). Electrostatic dust removal using adsorbed moisture–assisted charge induction for sustainable operation of solar panels. *Science Advances*, *8*(10), eabm0078. <https://doi.org/10.1126/sciadv.abm0078>
- Paulot, F., Ginoux, P., Cooke, W. F., Donner, L. J., Fan, S., Lin, M.-Y., et al. (2016). Sensitivity of nitrate aerosols to ammonia emissions and to nitrate chemistry: Implications for present and future nitrate optical depth. *Atmospheric Chemistry and Physics*, *16*(3), 1459–1477. <https://doi.org/10.5194/acp-16-1459-2016>
- Pérez, C., Nickovic, S., Pejanovic, G., Baldasano, J. M., & Özsoy, E. (2006). Interactive dust-radiation modeling: A step to improve weather forecasts. *Journal of Geophysical Research*, *111*(D16), D16206. <https://doi.org/10.1029/2005JD006717>
- Peuch, V.-H., Engelen, R., Rixen, M., Dee, D., Flemming, J., Suttie, M., et al. (2022). The Copernicus atmosphere monitoring service: From research to operations. *Bulletin of the American Meteorological Society*, *103*(12), E2650–E2668. <https://doi.org/10.1175/BAMS-D-21-0314.1>
- Platnick, S., King, M., & Hubanks, P. (2017a). MODIS/Aqua Aerosol Cloud Water Vapor Ozone Daily L3 Global 1Deg CMG [Dataset]. *NASA MODIS Adaptive Processing System, Goddard Space Flight Center*. https://doi.org/10.5067/MODIS/MYD08_D3.061
- Platnick, S., King, M., & Hubanks, P. (2017b). MODIS/Terra Aerosol Cloud Water Vapor Ozone Daily L3 Global 1Deg CMG [Dataset]. *NASA MODIS Adaptive Processing System, Goddard Space Flight Center*. https://doi.org/10.5067/MODIS/MOD08_D3.061
- Pollard, R. T., Rhines, P. B., & Thompson, R. O. R. Y. (1973). The deepening of the wind-mixed layer. *Geophysical Fluid Dynamics*, *4*(4), 381–404. <https://doi.org/10.1080/03091927208236105>
- Pourasl, H. H., Barenji, R. V., & Khojastehzad, V. M. (2023). Solar energy status in the world: A comprehensive review. *Energy Reports*, *10*, 3474–3493. <https://doi.org/10.1016/j.egy.2023.10.022>
- Pu, B., & Ginoux, P. (2016). The impact of the Pacific Decadal Oscillation on springtime dust activity in Syria. *Atmospheric Chemistry and Physics*, *16*(21), 13431–13448. <https://doi.org/10.5194/acp-16-13431-2016>
- Pu, B., & Ginoux, P. (2018). How reliable are CMIP5 models in simulating dust optical depth? *Atmospheric Chemistry and Physics*, *18*(16), 12491–12510. <https://doi.org/10.5194/acp-18-12491-2018>
- Pu, B., Ginoux, P., Guo, H., Hsu, N. C., Kimball, J., Marticorena, B., et al. (2020). Retrieving the global distribution of the threshold of wind erosion from satellite data and implementing it into the Geophysical Fluid Dynamics Laboratory land-atmosphere model (GFDL AM4.0/LM4.0). *Atmospheric Chemistry and Physics*, *20*(1), 55–81. <https://doi.org/10.5194/acp-20-55-2020>
- Pu, B., Ginoux, P., Kapnick, S. B., & Yang, X. (2019). Seasonal prediction potential for springtime dustiness in the United States. *Geophysical Research Letters*, *46*(15), 9163–9173. <https://doi.org/10.1029/2019GL083703>
- Pu, B., & Jin, Q. (2021). A record-breaking Trans-Atlantic African dust plume associated with atmospheric circulation extremes in June 2020. *Bulletin of the American Meteorological Society*, *102*(7), E1340–E1356. <https://doi.org/10.1175/BAMS-D-21-0014.1>
- Randles, C. A., da Silva, A. M., Buchard, V., Colarco, P. R., Darmenov, A., Govindaraju, R., et al. (2017). The MERRA-2 aerosol reanalysis, 1980 onward. Part I: System description and data assimilation evaluation. *Journal of Climate*, *30*(17), 6823–6850. <https://doi.org/10.1175/JCLI-D-16-0609.1>
- Reddy, M. S., Boucher, O., Bellouin, N., Schulz, M., Balkanski, Y., Dufresne, J.-L., & Mai, P. (2005). Estimates of global multicomponent aerosol optical depth and direct radiative perturbation in the Laboratoire de Météorologie Dynamique general circulation model. *Journal of Geophysical Research*, *110*(D10), D10S16. <https://doi.org/10.1029/2004JD004757>
- Rémy, S., Kipling, Z., Flemming, J., Boucher, O., Nabat, P., Michou, M., et al. (2019). Description and evaluation of the tropospheric aerosol scheme in the European Centre for Medium-Range Weather Forecasts (ECMWF) integrated forecasting system (IFS-AER, cycle 45R1). *Geoscientific Model Development*, *12*(11), 4627–4659. <https://doi.org/10.5194/gmd-12-4627-2019>
- Rémy, S., Kipling, Z., Huijnen, V., Flemming, J., Nabat, P., Michou, M., et al. (2022). Description and evaluation of the tropospheric aerosol scheme in the Integrated Forecasting System (IFS-AER, cycle 47R1) of ECMWF. *Geoscientific Model Development*, *15*(12), 4881–4912. <https://doi.org/10.5194/gmd-15-4881-2022>
- Rodwell, M. J., & Jung, T. (2008). Understanding the local and global impacts of model physics changes: An aerosol example. *Quarterly Journal of the Royal Meteorological Society*, *134*(635), 1479–1497. <https://doi.org/10.1002/qj.298>
- Rubin, J. I., Reid, J. S., Hansen, J. A., Anderson, J. L., Collins, N., Hoar, T. J., et al. (2016). Development of the Ensemble Navy Aerosol Analysis Prediction System (ENAAAPS) and its application of the Data Assimilation Research Testbed (DART) in support of aerosol forecasting. *Atmospheric Chemistry and Physics*, *16*(6), 3927–3951. <https://doi.org/10.5194/acp-16-3927-2016>
- Sarver, T., Al-Qaraghuli, A., & Kazmerski, L. L. (2013). A comprehensive review of the impact of dust on the use of solar energy: History, investigations, results, literature, and mitigation approaches. *Renewable and Sustainable Energy Reviews*, *22*, 698–733. <https://doi.org/10.1016/j.rser.2012.12.065>

- Sayer, A. M., Hsu, N. C., Lee, J., Kim, W. V., & Dutcher, S. T. (2019). Validation, stability, and consistency of MODIS Collection 6.1 and VIIRS version 1 deep blue aerosol data over land. *Journal of Geophysical Research: Atmospheres*, *124*(8), 4658–4688. <https://doi.org/10.1029/2018JD029598>
- Schroedter-Homscheidt, M., Oumbe, A., Benedetti, A., & Morcrette, J.-J. (2013). Aerosols for concentrating solar electricity production forecasts: Requirement quantification and ECMWF/MACCS aerosol forecast assessment. *Bulletin of the American Meteorological Society*, *94*(6), 903–914. <https://doi.org/10.1175/BAMS-D-11-00259.1>
- Sekiyama, T. T., Yumimoto, K., Tanaka, T. Y., Nagao, T., Kikuchi, M., & Murakami, H. (2016). Data assimilation of Himawari-8 aerosol observations: Asian dust forecast in June 2015. *SOLA*, *12*(0), 86–90. <https://doi.org/10.2151/sola.2016-020>
- Shao, Y., Raupach, M. R., & Findlater, P. A. (1993). Effect of saltation bombardment on the entrainment of dust by wind. *Journal of Geophysical Research*, *98*(D7), 12719–12726. <https://doi.org/10.1029/93JD00396>
- Shimizu, A., Sugimoto, N., Matsui, I., Arao, K., Uno, I., Murayama, T., et al. (2004). Continuous observations of Asian dust and other aerosols by polarization lidars in China and Japan during ACE-Asia. *Journal of Geophysical Research*, *109*(D19), 2002JD003253. <https://doi.org/10.1029/2002JD003253>
- Sugimoto, N., Matsui, I., Shimizu, A., Nishizawa, T., Hara, Y., Xie, C., et al. (2008). In U. N. Singh, K. Asai, & A. Jayaraman (Eds.), *Lidar network observations of tropospheric aerosols* (p. 71530A). <https://doi.org/10.1117/12.806540>
- Takemura, T., Egashira, M., Matsuzawa, K., Ichijo, H., O'ishi, R., & Abe-Ouchi, A. (2009). A simulation of the global distribution and radiative forcing of soil dust aerosols at the Last Glacial Maximum. *Atmospheric Chemistry and Physics*, *9*(9), 3061–3073. <https://doi.org/10.5194/acp-9-3061-2009>
- Takemura, T., Okamoto, H., Maruyama, Y., Numaguti, A., Higurashi, A., & Nakajima, T. (2000). Global three-dimensional simulation of aerosol optical thickness distribution of various origins. *Journal of Geophysical Research*, *105*(D14), 17853–17873. <https://doi.org/10.1029/2000JD900265>
- Tegen, I., & Fung, I. (1994). Modeling of mineral dust in the atmosphere: Sources, transport, and optical thickness. *Journal of Geophysical Research*, *99*(D11), 22897–22914. <https://doi.org/10.1029/94JD01928>
- Terradellas, E. (2022). Model inter-comparison and evaluation of dust forecasts.
- Textor, C., Schulz, M., Guibert, S., Kinne, S., Balkanski, Y., Bauer, S., et al. (2006). Analysis and quantification of the diversities of aerosol life cycles within AeroCom. *Atmospheric Chemistry and Physics*, *6*(7), 1777–1813. <https://doi.org/10.5194/acp-6-1777-2006>
- Textor, C., Schulz, M., Guibert, S., Kinne, S., Balkanski, Y., Bauer, S., et al. (2007). The effect of harmonized emissions on aerosol properties in global models—An AeroCom experiment. *Atmospheric Chemistry and Physics*, *7*(17), 4489–4501. <https://doi.org/10.5194/acp-7-4489-2007>
- Thiébaux, J., Rogers, E., Wang, W., & Katz, B. (2003). A new high-resolution blended real-time global sea surface temperature analysis. *Bulletin of the American Meteorological Society*, *84*(5), 645–656. <https://doi.org/10.1175/BAMS-84-5-645>
- Tindan, J. Z., Jin, Q., & Pu, B. (2023). Understanding day–night differences in dust aerosols over the dust belt of North Africa, the Middle East, and Asia. *Atmospheric Chemistry and Physics*, *23*(9), 5435–5466. <https://doi.org/10.5194/acp-23-5435-2023>
- Tompkins, A. M. (2005). A revised cloud scheme to reduce the sensitivity to vertical resolution. In *ECMWF Research Department Technical Memorandum* (Vol. 599, p. 25).
- Ukhov, A., Ahmadov, R., Grell, G., & Stenchikov, G. (2021). Improving dust simulations in WRF-Chem v4.1.3 coupled with the GOCART aerosol module. *Geoscientific Model Development*, *14*(1), 473–493. <https://doi.org/10.5194/gmd-14-473-2021>
- VIIRS Atmosphere Science Team, S. (2023a). VIIRS/NOAA20 Deep Blue Level 3 daily aerosol data, 1 degree x1 degree grid [Dataset]. *NASA Level 1 and Atmosphere Archive and Distribution System Distributed Active Archive Center*. https://doi.org/10.5067/VIIRS/AERDB_D3_VIIRS_NOAA20.002
- VIIRS Atmosphere Science Team, S. (2023b). VIIRS/SNPP Deep Blue Level 3 daily aerosol data, 1 degree x1 degree grid [Dataset]. *NASA Level 1 and Atmosphere Archive and Distribution System Distributed Active Archive Center*. https://doi.org/10.5067/VIIRS/AERDB_D3_VIIRS_SNPP.002
- Wang, H., Zhang, X. Y., Wang, P., Peng, Y., Zhang, W. J., Liu, Z. D., et al. (2022). Chemistry-weather interacted model system GRAPES_Meso5.1/CUACE CW V1.0: Development, evaluation and application in better haze/fog prediction in China. *Journal of Advances in Modeling Earth Systems*, *14*(12). <https://doi.org/10.1029/2022MS003222>
- Wang, J., Bhattacharjee, P. S., Tallapragada, V., Lu, C.-H., Kondragunta, S., da Silva, A., et al. (2018). The implementation of NEMS GFS Aerosol Component (NGAC) Version 2.0 for global multispecies forecasting at NOAA/NCEP—Part 1: Model descriptions. *Geoscientific Model Development*, *11*(6), 2315–2332. <https://doi.org/10.5194/gmd-11-2315-2018>
- Wesely, M., & Hicks, B. (2000). A review of the current status of knowledge on dry deposition. *Atmospheric Environment*, *34*(12–14), 2261–2282. [https://doi.org/10.1016/S1352-2310\(99\)00467-7](https://doi.org/10.1016/S1352-2310(99)00467-7)
- Winker, D. M., Pelon, J., Coakley, J. A., Ackerman, S. A., Charlson, R. J., Colarco, P. R., et al. (2010). The CALIPSO mission. *Bulletin of the American Meteorological Society*, *91*(9), 1211–1230. <https://doi.org/10.1175/2010BAMS3009.1>
- Woodward, S. (2001). Modeling the atmospheric life cycle and radiative impact of mineral dust in the Hadley Centre climate model. *Journal of Geophysical Research*, *106*(D16), 18155–18166. <https://doi.org/10.1029/2000JD900795>
- Xu, K.-M., & Randall, D. A. (1996). A semiempirical cloudiness parameterization for use in climate models. *Journal of the Atmospheric Sciences*, *53*(21), 3084–3102. [https://doi.org/10.1175/1520-0469\(1996\)053<3084:ASCPFU>2.0.CO;2](https://doi.org/10.1175/1520-0469(1996)053<3084:ASCPFU>2.0.CO;2)
- Yu, Y., Notaro, M., Liu, Z., Wang, F., Alkolibi, F., Fadda, E., & Bakhrjy, F. (2015). Climatic controls on the interannual to decadal variability in Saudi Arabian dust activity: Toward the development of a seasonal dust prediction model: Saudi Arabian dust prediction. *Journal of Geophysical Research: Atmospheres*, *120*(5), 1739–1758. <https://doi.org/10.1002/2014JD022611>
- Yue, M., Dong, X., Wang, M., Emmons, L. K., Liang, Y., Tong, D., et al. (2023). Modeling the air pollution and aerosol-PBL interactions over China using a variable-resolution global model. *Journal of Geophysical Research: Atmospheres*, *128*(22), e2023JD039130. <https://doi.org/10.1029/2023JD039130>
- Zeng, Y., Wang, M., Zhao, C., Zhu, Y., Rosenfeld, D., & Huang, K.-E. (2023). Extremely high concentrations of ice particles in East Asian dust-infused baroclinic storm (DIBS) cirrus shield: Dominant role of dust ice nucleation effect. *Journal of Geophysical Research: Atmospheres*, *128*(6), e2022JD038034. <https://doi.org/10.1029/2022JD038034>
- Zhang, J., Jian, S., Xueshun, S., Yong, S., Zhanshan, M., Hao, J., et al. (2023). Key model technologies of CMA-GFS V4.0 and application to operational forecast. *Journal of Applied Meteorological Science*, *34*(5), 513–526. <https://doi.org/10.11898/1001-7313.20230501>
- Zhang, J. A., Nolan, D. S., Rogers, R. F., & Tallapragada, V. (2015). Evaluating the impact of improvements in the boundary layer parameterization on Hurricane intensity and structure forecasts in HWRF. *Monthly Weather Review*, *143*(8), 3136–3155. <https://doi.org/10.1175/MWR-D-14-00339.1>
- Zhang, L., Gong, S., Zhao, T., Zhou, C., Wang, Y., Li, J., et al. (2021). Development of WRF/CUACE v1.0 model and its preliminary application in simulating air quality in China. *Geoscientific Model Development*, *14*(2), 703–718. <https://doi.org/10.5194/gmd-14-703-2021>

- Zhang, L., Montuoro, R., McKeen, S. A., Baker, B., Bhattacharjee, P. S., Grell, G. A., et al. (2022). Development and evaluation of the aerosol forecast member in the national center for environment prediction (NCEP)'s global ensemble forecast system (GEFS-Aerosols v1). *Geoscientific Model Development*, *15*(13), 5337–5369. <https://doi.org/10.5194/gmd-15-5337-2022>
- Zhang, X., Zhao, L., Tong, D., Wu, G., Dan, M., & Teng, B. (2016). A systematic review of global desert dust and associated human health effects. *Atmosphere*, *7*(12), 158. <https://doi.org/10.3390/atmos7120158>
- Zhou, L., Lin, S.-J., Chen, J.-H., Harris, L. M., Chen, X., & Rees, S. L. (2019). Toward convective-scale prediction within the next generation global prediction system. *Bulletin of the American Meteorological Society*, *100*(7), 1225–1243. <https://doi.org/10.1175/BAMS-D-17-0246.1>